

Immersed granular collapse: from viscous to free-fall unsteady granular flows

Laurent Lacaze^{1,†}, Joris Bouteloup¹, Benjamin Fry¹ and Edouard Izard¹

¹Institut de Mécanique des Fluides de Toulouse (IMFT), Université de Toulouse, CNRS, Toulouse 31400, France

(Received 16 April 2019; revised 7 October 2020; accepted 2 December 2020)

The collapse of a granular column in a liquid is investigated using numerical simulations. From previous experimental studies, it has been established that the dynamics of the collapse is mostly influenced by the Stokes number St , comparing grain inertia and viscous fluid dissipation, and the initial volume fraction of the granular column ϕ_i . However, the full characterization of the collapse in the (St, ϕ_i) plane is still missing, restricting its modelling as a physical process for geophysical applications. Only numerical tools can allow the variation over the parameter space (St, ϕ_i) that is hardly reachable in experiments as well as a full description of the granular phase that plays a major role in dense granular flows. For this purpose, a dedicated numerical model is used including a discrete element method to resolve the granular phase. The specific objectives of the paper are then twofold: (i) the characterization of the dynamics of the collapse and its final deposit with respect to (St, ϕ_i) to complement available experimental data, and (ii) the description of the granular rheology according to these two dimensionless numbers including dilatancy effects. A simple predictive model stems from the obtained results, allowing one to explain the evolution of the final deposit with (St, ϕ_i) .

Key words: granular media, particle/fluid flow, rheology

1. Introduction

Destructive natural phenomena such as snow avalanches, landslides, rock falls and debris flows remain difficult to safeguard against. Given the complexity and the observed heterogeneity in dynamics of these gravity-driven and unsteady multiphase flows, it is natural to focus on canonical flows that can be controlled at the laboratory scale. For this purpose, several studies have been devoted to model configurations dealing with dry or wet granular flows.

[†] Email address for correspondence: laurent.lacaze@imft.fr

Among other configurations, the collapse of an initial granular column in air and over a horizontal surface, referred to as dry granular collapse, reveals the behaviour of an unsteady granular flow starting from an initial unstable rest state and evolving towards a final deposit. This configuration thus shares many key features with natural situations, and it has naturally become the topic of several studies. It should be noted that specific attention has been paid to the case of a dry monodisperse granular medium using laboratory experiments (Lajeunesse, Mangeney-Castelnaud & Vilotte 2004; Lube *et al.* 2004, 2005; Balmforth & Kerswell 2005; Lajeunesse, Monnier & Homsy 2005; Lacaze, Phillips & Kerswell 2008) or numerical modelling at different scales (Mangeney-Castelnaud *et al.* 2005; Zenit 2005; Staron & Hinch 2005, 2007; Lacaze & Kerswell 2009; Lagrée, Staron & Popinet 2011; Girolami *et al.* 2012; Ionescu *et al.* 2015). Even for such a canonical design, the dynamics of the collapse remains not fully understood, like many dry dense granular flows. Surprisingly, some simple features have nevertheless been observed in all these studies. In particular, the characterization of the dynamics and of the final deposit has shown that the collapse is mostly controlled by the aspect ratio $a = H_i/L_i$ of the initial column, with H_i and L_i its initial height and its initial horizontal length, respectively.

Complexity has been increasingly added to the dry granular collapse to incorporate observable features in natural configurations, such as polydispersity or complex grain shape (Phillips *et al.* 2006; Degaetano, Lacaze & Phillips 2013; Cabrera & Estrada 2019), erodible bottom (Crosta, Imposimato & Roddeman 2009; Mangeney *et al.* 2010) or the influence of the surrounding fluid (Roche *et al.* 2011; Rondon, Pouliquen & Aussillous 2011; Topin *et al.* 2012; Bougouin & Lacaze 2018; Jing *et al.* 2018, 2019). In the latter situation, it has been highlighted that, as well as a , the initial volume fraction ϕ_i (Rondon *et al.* 2011) and Stokes number St (Bougouin & Lacaze 2018) can also play a significant role in the dynamics of collapse. In other words, for given granular material and aspect ratio, the surrounding fluid can affect the granular collapse because of its influence on falling grain inertia through viscous dissipation, i.e. the St number, but also due to the initial compaction of the granular column, i.e. ϕ_i .

The specific contributions of both St and ϕ_i to the immersed granular collapse now require to be characterized. For this purpose, a full picture of the influence of (St, ϕ_i) needs to be provided, as up to now only a limited set of dimensionless parameters has been considered. In particular, the role of ϕ_i observed at small St (Rondon *et al.* 2011) – and presumed to be negligible at large St according to the results obtained in dry configuration – suggests a combined influence of (St, ϕ_i) which would both originate from fluid viscosity. Thus, the influence of ϕ_i has to be clarified as a function of St . Moreover, modelling granular collapse from physical analysis is required for larger-scale situations. This means, in particular, extracting pertinent continuous models for the granular phase including its rheological behaviour. The granular collapse has already been shown to be an attractive test case for rheological models in the case of dry configuration (Lacaze & Kerswell 2009). It has to be extended to the case of immersed situations.

In order to achieve these objectives, fluid–particle properties have to be continuously varied, and fluid–particle stresses have to be known. These objectives then suffer experimental limitations, which, for now, can only be achieved using numerical simulations. Here, a volume-averaged Navier–Stokes/discrete element method (VANS/DEM) coupling approach is used. This approach is referred to as the mesoscale approach in the following as it allows one to solve the fluid phase at a scale slightly larger than the grain scale. This provides a reasonable scale of description to model laboratory-scale configurations, keeping the Lagrangian description of individual grains. It has therefore often been used when dealing with immersed granular flows such as,

among others, the immersed simple shear flow (Trulsson, Andreotti & Claudin 2012) and sediment transport (Maurin *et al.* 2015; Charru *et al.* 2016; Pähz & Durán 2018). Even if most of the dynamics of the system is resolved with this approach, the properties and dynamics of the fluid flow in between grains remains modelled, and thus requires closure terms. This approach has nevertheless proved to be relevant for the above-mentioned configurations and, particularly, to provide the relevant mechanisms, allowing us to improve our understanding of the physics of these systems. This means that most of the required subscale physics of the fluid phase is captured by these closure models. Accordingly, this remains a pertinent scale approach to reach the main objectives depicted previously.

The paper is organized as follows. The numerical VANS/DEM method used in the paper, the collapse set-up and the dimensionless parameters are presented in § 2. In order to discuss the reliability of the mesoscale model used in this paper, an alternative resolved numerical approach for the fluid phase, solving part of the subscale physics, has also been tested. Results, comparisons and limitations are discussed in supplementary material available at <https://doi.org/10.1017/jfm.2020.1088>. The influence of (St, ϕ_i) on the dynamics of the collapse and its final rest state is then characterized in § 3, with specific attention paid to the prevailing role of ϕ_i when decreasing St . In § 4, the rheology of the granular material is extracted and characterized as a function of (St, ϕ_i) , in the spirit of the μ - I model for dense granular flows. Prior to concluding, the link between the proposed rheological model and the obtained final deposit for immersed granular collapse is discussed in terms of a simplified predictive model in § 5.

2. A mesoscale approach for granular collapse modelling

The VANS/DEM numerical method used in the following has been explained in detail in Charru *et al.* (2016). The method is thus only briefly recalled for the record. Nevertheless, we pay attention here to highlighting the terms that require closure models and the strategy adopted accordingly (see also the supplementary material for a discussion on these models). The physical set-up and the associated dimensionless parameters used are then given.

2.1. Granular phase: discrete element method

The dynamics of the granular phase is solved using a classical DEM. The motion of each solid particle j , with $j \in [1, N_p]$ (with N_p being the number of particles), submitted to gravitational acceleration, solid contact force with other particles and hydrodynamics force induced by the surrounding fluid, is obtained by integrating Newton's equations for linear and angular momentum of a solid sphere of mass m_j ,

$$m_j \frac{d\mathbf{v}_j}{dt} = m_j \mathbf{g} + \mathbf{F}_j^h + \sum_{k \neq j} \mathbf{F}_{kj}^c, \quad \frac{m_j d_j^2 d\boldsymbol{\omega}_j}{10 dt} = \boldsymbol{\Gamma}_j^h + \sum_{k \neq j} \boldsymbol{\Gamma}_{kj}^c, \quad (2.1a,b)$$

where \mathbf{v}_j and $\boldsymbol{\omega}_j$ correspond to the linear velocity and the angular velocity, respectively, \mathbf{F}_j^h and $\boldsymbol{\Gamma}_j^h$ are the hydrodynamic force and torque exerted on each particle j , respectively, and \mathbf{F}_{kj}^c and $\boldsymbol{\Gamma}_{kj}^c$ are the solid contact force and torque, respectively, exerted by particle k on particle j if they are in contact. Note that, with the formulation just mentioned, \mathbf{F}_j^h then includes the buoyancy contribution. The model of the hydrodynamics force on each particle will be specified in the next section.

Solid contacts between particles are modelled using a soft sphere approach, i.e. by allowing a small overlap between particles to mimic the deformation of real grains. This overlap is then used to calculate the contact force between grains, using a linear spring–dashpot model. The tangential force is limited by a Coulomb threshold allowing sliding between grains. Details of the model can be found in Izard, Bonometti & Lacaze (2014). We only recall that the solid contact is then parametrized by the coefficient of restitution e and the coefficient of friction μ_p between the two particles in contact and the stiffness of the considered material k_n , or equivalently the contact time t_c . In the case of granular material, we impose $t_c \ll \sqrt{d/g}$ to ensure rigidity of the material for the dry situation (Baran *et al.* 2006). Here, $t_c = 2 \times 10^{-3} \sqrt{d/g}$, or equivalently the stiffness of the particle is $k_n = 2 \times 10^5 \text{ mg/d}$. Note that, in such a limit, the stiffness of the material no longer influences the dynamics of the granular material (Baran *et al.* 2006). In fact, we also have $t_c \ll \rho d^2/\eta$, where ρ and η are the density and the viscosity of the surrounding fluid, respectively. The latter constraint ensures that the contact time is smaller than the diffusive time scale in the vicinity of the moving particle.

2.2. Fluid phase: volume-averaged Navier–Stokes model

The fluid phase is solved at a scale larger than the grain size, as sketched in figure 1 for a two-dimensional (2-D) cross-section of the 3-D physical domain. For this purpose, the fluid-phase equations to be resolved are derived from the Navier–Stokes (NS) equations spatially averaged over a spatial scale larger than the grain size (Jackson 2000). In other words, the NS equations are averaged over a volume \mathcal{V}_f of fluid contained in a volume of reference \mathcal{V} larger than a solid particle and similar to the mesh cell volume (see figure 1 for a sketch). The VANS mass and momentum equations read (Jackson 2000)

$$\frac{\partial \varepsilon}{\partial t} + \nabla \cdot (\varepsilon \langle \mathbf{u} \rangle_f) = 0, \tag{2.2}$$

$$\varepsilon \frac{D \langle \mathbf{u} \rangle_f}{Dt} = \varepsilon \mathbf{g} + \frac{1}{\rho} \nabla \cdot \mathbf{S} - \frac{1}{\rho} n \langle \mathbf{f}_{p/f} \rangle_p, \tag{2.3}$$

where $\varepsilon = 1 - \phi$ is the local fluid volume fraction (ϕ is the particle volume fraction), $\langle \cdot \rangle_f$ and $\langle \cdot \rangle_p$ denote the average operator over the fluid phase and particle phase within the volume \mathcal{V} , respectively, and D/Dt is a fluid material derivative and is defined accordingly with respect to the fluid velocity $\langle \mathbf{u} \rangle_f$ as $D/Dt = \partial/\partial t + \langle \mathbf{u} \rangle_f \cdot \nabla$. The fluid–particle interaction force averaged over the particles within \mathcal{V} is denoted $n \langle \mathbf{f}_{p/f} \rangle_p$, with n the number of particles per unit volume. Finally, \mathbf{S} is an effective stress tensor for the fluid, which has to be specified. Note that using this volume-averaged formulation, different contributions emerge in the stress \mathbf{S} , including the average fluid stress tensor over \mathcal{V}_f as well as what is referred to as the traction term in Jackson (2000), defined at the interface between the particles and the fluid.

The fluid–particle interaction force $n \langle \mathbf{f}_{p/f} \rangle_p$ is simply related to the hydrodynamics force on each grain \mathbf{F}_j^h in the Lagrangian formulation (2.1a,b) as

$$n \langle \mathbf{f}_{p/f} \rangle_p = \frac{1}{\mathcal{V}} \sum_{j \in \mathcal{V}} \mathbf{F}_j^h. \tag{2.4}$$

In the VANS/DEM model, particle–fluid interaction is not resolved at the grain scale and \mathbf{F}_j^h , and thus $n \langle \mathbf{f}_{p/f} \rangle_p$, have therefore to be modelled. According to Jackson (2000),

Immersed granular collapse

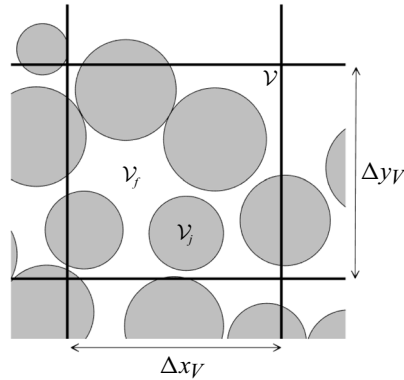


Figure 1. Sketch of the spatial scales used for the VANS/DEM approach in a 2-D (x, y) cross-section. Here $(\Delta x_V, \Delta y_V)$ defines the grid size for the fluid phase resolution in the 2-D plane. Grey disks are the 2-D slice through the three-dimensional (3-D) spherical grain of diameter d in this 2-D cross-section.

the fluid–particle interaction force can be split into a buoyancy contribution and a local interaction force. For the sake of simplicity, we assume that the remaining contribution is only a drag force. We thus write

$$n\langle \mathbf{f}_{p/f} \rangle_p = \phi \nabla \cdot \mathbf{S} + n\mathbf{F}_D^M, \quad (2.5)$$

where \mathbf{F}_D^M corresponds to a drag model force at the scale of the grain, superscript M standing for ‘modelled’. We choose in the following to model this drag contribution as (see, for instance, Richardson & Zaki 1954; Maurin *et al.* 2015)

$$n\mathbf{F}_D^M = \frac{18\eta}{d^2} \phi (1 - \phi)^{-\xi} \left(1 + \frac{1}{60} Re_p \right) (\langle \mathbf{v} \rangle_p - \langle \mathbf{u} \rangle_f), \quad (2.6)$$

with $Re_p = \rho d |\langle \mathbf{v} \rangle_p - \langle \mathbf{u} \rangle_f| / \eta$, and ξ is a constant whose value lies in the interval $[1, 3]$. Note that such a force model does not provide any torque on the particle that would be induced by the fluid; thus $\mathbf{\Gamma}_j^h = \mathbf{0}$ in (2.1a,b) for this specific method. The only torque applied to each grain therefore comes from solid contact. This is quite a crude approximation, but it provides the simplest model leading to the expected dynamics of the collapse (see the supplementary material).

Moreover, we assume that the deviatoric part of the stress can be simply written as a generalized viscous stress, leading to a total stress \mathbf{S} of the form

$$\mathbf{S} = -\langle p \rangle_f \mathbf{I} + \eta_{eff} (\nabla \langle \mathbf{u} \rangle + {}^T \nabla \langle \mathbf{u} \rangle) \equiv -\langle p \rangle_f \mathbf{I} + \eta_{eff}^M (\nabla \langle \mathbf{u} \rangle + {}^T \nabla \langle \mathbf{u} \rangle), \quad (2.7)$$

where $\langle \cdot \rangle$ stands for an average over the mixture and $\langle \mathbf{u} \rangle = \varepsilon \langle \mathbf{u} \rangle_f + \phi \langle \mathbf{v} \rangle_p$ is its average velocity, with $\phi \langle \mathbf{v} \rangle_p = (1/\mathcal{V}) \sum_{j \in \mathcal{V}} \mathcal{V}_j \mathbf{v}_j$. The viscosity η_{eff} is an effective viscosity. This viscosity has to be modelled and will thus be denoted $\eta_{eff} \equiv \eta_{eff}^M$.

Note that, in (2.7), mixture velocity has been chosen instead of the fluid velocity to model the viscous deviatoric stress component. In the literature, both choices can be found as long as they provide an actual deviatoric tensor for the viscous stress (for a review, see Jackson 2000). Then, if the fluid velocity is chosen, its trace contribution has to be subtracted, as the fluid phase is not divergence-free in the case of the fluid (Baumgarten & Kamrin 2019). Using the mixture velocity allows one to satisfy straightforwardly the

previous constraint, as it is divergence-free, and moreover it has been shown to appear quite naturally in the case of dilute Stokes flow (Zhang & Prosperetti 1997; Jackson 2000). The latter approach has also been used to describe dense situations (Guazzelli & Pouliquen 2018). This definition has thus been chosen here regarding the state of our knowledge. Moreover, the following model will be used for the effective viscosity,

$$\frac{\eta_{eff}^M}{\eta} = 1 + \frac{5}{2}\phi + 7.6\phi^2 + \zeta\phi^3, \quad (2.8)$$

where we recognize the Einstein viscosity at $O(\phi)$, the Batchelor viscosity for hard spheres at $O(\phi^2)$, and an extra $O(\phi^3)$ term to account for higher-order correction in such a dense configuration.

In most of the simulations discussed in this paper, $\xi = 1$ in (2.6) and $\eta_{eff}^M/\eta = 1 + 5\phi/2$ in (2.8). However, a discussion on the influence of these models is given in § 3.4, including $\xi = 2$, $\xi = 3$ and higher-order viscosity terms. Moreover, a resolved numerical approach at the grain scale has been used to show the relevance of these different models and to obtain an estimation of $\zeta \approx 16$ in (2.8) for the flows studied in this work (see the supplementary material).

The VANS equations (2.2) and (2.3) are solved numerically to obtain $\langle \mathbf{u} \rangle_f$ and $\langle p \rangle_f$ on a regular mesh grid $\Delta x_V = \Delta y_V = \Delta z_V = 2d$, where the cell volume matches the elementary volume \mathcal{V} (see figure 1). Note that we take advantage of the incompressibility of the mixture (fluid plus grains) to solve a divergence-free equation for the mixture phase instead of (2.2), allowing the use of a standard numerical algorithm developed for incompressible flows. The required ε and $\langle \mathbf{v} \rangle_p$ are obtained by averaging DEM results over the fluid cell. For more details on the numerical algorithm, the reader can refer to Charru *et al.* (2016).

2.3. Set-up and dimensionless numbers

A typical sketch of the configuration considered in this study is shown in figure 2. The computational domain consists of a rectangular box (L_x, L_y, L_z) in (x, y, z) with (x, y) the main propagation plane, y being opposed to gravity (see figure 2), and z is the third, out-of-plane, direction. Boundary conditions for both the fluid phase and the granular phase are periodic in the z direction. For the fluid phase, a no-slip condition is imposed at the walls located at $x = 0$ and $y = 0$, while a slip condition is imposed at the walls located at $x = L_x$ and $y = L_y$, $\partial \langle \mathbf{u} \rangle_f / \partial \mathbf{n} = 0$, with \mathbf{n} being the normal to the wall. Grains of diameter d are glued on the bottom plane – on a square grid centred at $y = 0$ – to prevent the granular material from rolling on the bottom.

At the left-hand side of the domain, $x = 0$, a rectangular column of base (L_i, L_z) is filled up to a height H_i with N_p spherical grains of mean diameter d and the same density ρ_p (see figure 2a). Only a small dispersion ($\pm 5\%$ in diameter of a uniform distribution) is imposed onto the grain diameter to avoid a crystal-like pattern in the medium while keeping a monodisperse behaviour, i.e. no segregation is observed for such small dispersion in grain diameter. The geometry of the system is unchanged for all simulations. In particular, the aspect ratio of the initial column is set to $a = H_i/L_i = 0.5$, i.e. $H_i = L_i/2$, as its influence on the collapse has already been reported in several studies. The dimensionless base length of the column is $L_i/d = 64$. The dimensionless size of the computational domain is such that $L_x/d \approx 192$, $L_y/d \approx 51$ and $L_z/d = 8$.

At $t = 0$, the column is released in a liquid of density ρ and viscosity η . For $t > 0$, the granular medium first collapses during a so-called slumping phase, and eventually stops

Immersed granular collapse

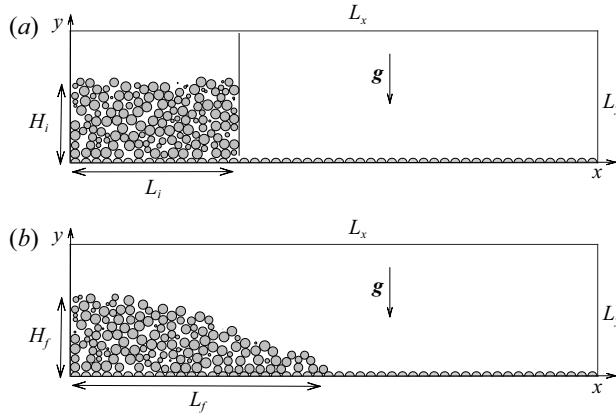


Figure 2. Sketch of the 3-D set-up in a 2-D streamwise (x, y) plane at a fixed z coordinate. Unit vector z is in the out-of-plane direction. (a) Initial configuration at $t = 0$ and (b) final deposit for $t \geq t_f$.

at a finite time $t = t_f$. The final deposit can be characterized by two lengths, say a final spreading length L_f and a final maximum height H_f (see figure 2b), or equivalently L_f and a deposit slope $\tan \alpha$, which will be defined later.

At the grain scale, the dynamics is controlled by several dimensionless parameters, including solid–solid interaction and fluid–solid interaction. For the solid–solid interaction, first, the dimensionless parameter characterizing the rigidity is defined as $\kappa = (\tau_i/t_c)^2$, with $\tau_i = d\sqrt{\rho_p/\Delta\rho g H_i}$ a characteristic time of rearrangement imposed by the granular pressure (see, for instance, GDR MiDi (2004); here the characteristic pressure is the granulostatic one at the bottom of the column using the apparent weight of the granular material $\Delta\rho = \rho_p - \rho_f$). The value of this parameter in the present simulations is $\kappa = 5 \times 10^5$ ensuring the rigidity of the material as mentioned previously (Da Cruz *et al.* 2005). In this rigid limit, the significant parameters characterizing the solid–solid interaction are then the coefficient of restitution e and the coefficient of friction μ_p . In the following, they are set to $e = 0.87$ and $\mu_p = 0.25$.

For the fluid–solid interaction in such a gravity-driven flow, two dimensionless parameters can be built upon the fluid and particle properties, say a Stokes number St and a density ratio r . The density ratio r is usually defined as $r = (\rho_p/\rho)^{1/2}$ and is kept constant in the following, $r = 1.6$, corresponding to glass into water, as mostly used in laboratory experiments. Its influence on the collapse has been reported in Bougouin & Lacaze (2018), and is beyond the scope of the present paper. The Stokes number St can be defined in different ways, and we choose here to follow Bougouin & Lacaze (2018) as

$$St = \frac{1}{18\sqrt{2}} \frac{(\rho_p \Delta\rho g d^3)^{1/2}}{\eta}. \quad (2.9)$$

In order to vary St , the viscosity of the fluid η is varied over five decades to range in $St \in [6 \times 10^{-3}, 60]$. This range of St allows one to cover both the viscous regime and the free-fall regime as defined in Courrech du Pont *et al.* (2003) and Cassar, Nicolas & Pouliquen (2005). Note that the validity of the model (2.8) for η_{eff}^M when increasing St in this range is probably questionable, as fluid inertia at the scale of the grains could become not negligible. However, the small-scale fluid-inertia contribution should be limited in a dense granular configuration, and mostly dominant close to the upper surface of the

a	L_i/d	L_z/d	ϕ_i	r	St
0.5	64	8	[0.57, 0.59, 0.63]	1.6	[6×10^{-3} , 60] (13 values evenly distributed on a log scale)

Table 1. Range of dimensionless parameters covered.

granular medium. This is therefore expected to decrease quickly in the granular medium and not to be a dominant effect in the present configuration. Fluid inertia is therefore only accounted for through the drag model (2.6).

At the scale of the initial column, beyond the initial aspect ratio a set constant in the present study (recall that we have set $a = 0.5$), the column is characterized by its initial volume fraction defined as

$$\phi_i = \frac{\sum_{j=1:N_p} \mathcal{V}_j}{L_i H_i L_z}, \quad (2.10)$$

with \mathcal{V}_j the volume of grain j . The volume fraction of the initial column ϕ_i is varied by modifying the filling procedure. We cover the range $\phi_i \in [0.57, 0.63]$. Note that the total number of grains is $N_p \approx 20\,000$ whose exact value depends on ϕ_i .

The set of dimensionless parameters used is collected together in table 1.

3. On the influence of St and ϕ_i on immersed granular collapses

3.1. Preliminary considerations and typical observations

Experimental observations of dry and immersed granular collapses are noticeably different, particularly concerning the influence of ϕ_i reported in both cases. Even if differences in the transient and the final profiles for varying ϕ_i were observed for the dry case in an almost similar configuration (Daerr & Douady 1999), they remain relatively small. Then the influence of ϕ_i was not discussed any longer in the literature for the case of dry granular collapse. On the other hand, when dealing with immersed granular flows, Rondon *et al.* (2011) reported the influence of ϕ_i as one of the dominant effects on the granular pile evolution. Their experiments were performed for $St = \{0.035, 0.065\}$ according to the definition (2.9), i.e. in a viscous regime at small St .

These experimental observations can be recovered using the VANS/DEM approach as reported in figure 3. In particular, one shows the temporal evolution of the dimensionless height profiles of the granular material $h(x/d)/d$ for different values of (St, ϕ_i) . We focus here on $St = \{6 \times 10^{-3}, 60\}$ and $\phi_i = \{0.57, 0.63\}$. In a viscous-dominated situation, $St = 6 \times 10^{-3}$ (figure 3a,b), ϕ_i clearly influences both the dynamics and the final rest state of the collapse. In particular, the initiation of the collapse is clearly delayed for the dense initial situation $\phi_i = 0.63$ with an initiation of the collapse at the right upper corner of the initial column (figure 3b) while no delay is observed for the initial loose configuration for which the collapse is initiated at the right bottom corner (figure 3a). Moreover, the spreading length is significantly more important for the loose situation. These observations are in qualitative agreement with experimental observations at small St (Rondon *et al.* 2011). On the other hand, for a particle-inertia (free-fall) configuration, $St = 60$ (figure 3c,d), the influence of ϕ_i is less obvious. Certainly, the spreading length is not affected, which explained why no influence of ϕ_i was reported in experimental studies

Immersed granular collapse

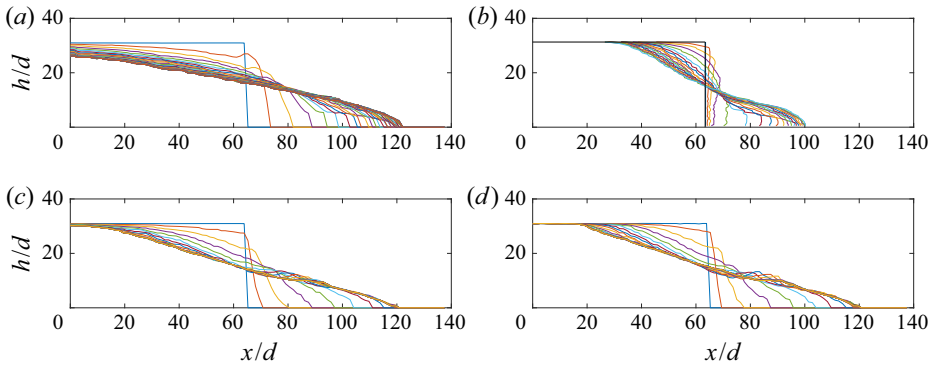


Figure 3. Dimensionless height profiles $h(x/d)/d$ of the granular medium at different times: (a) $(St, \phi_i) = (6 \times 10^{-3}, 0.57)$ and time step $\Delta t\sqrt{g/d} = 150$; (b) $(St, \phi_i) = (6 \times 10^{-3}, 0.63)$ and time step $\Delta t\sqrt{g/d} = 150$; (c) $(St, \phi_i) = (60, 0.57)$ and time step $\Delta t\sqrt{g/d} = 15$; and (d) $(St, \phi_i) = (60, 0.63)$ and time step $\Delta t\sqrt{g/d} = 15$.

dealing with dry collapse. However, a small difference can be observed close to the summit of the deposit. This observation reflects results reported by Daerr & Douady (1999).

The numerical results reported in figure 3 highlight the relevance of the mesoscale approach to provide the main behaviours obtained in previous experiments.

3.2. Granular morphology during collapse: a simple geometrical model

In order to highlight similarities and differences of collapses in the range of (St, ϕ_i) considered here, the time-dependant position of the centre of mass of the granular material (X_g, Y_g) in the (x, y) plane is first considered as a relevant quantifier of its morphology during collapse. For this purpose, the trajectory of the centre of mass $(2Y_g - L_i)/L_i, (2X_g - L_i)/L_i$ during the collapse, i.e. for $t \in [0, t_f]$, is shown in figure 4 for different values of (St, ϕ_i) . Surprisingly, one observes that all trajectories remarkably collapse onto a single curve prior to reaching the final deposit. The only difference between all the cases considered here is the position at which the trajectory of a given (St, ϕ_i) stops onto this universal curve (see, in particular, the inset of figure 4). Note that this observation confirms the experimental results reported by Bougouin & Lacaze (2018) for constant $\phi_i \approx 0.64$. Obviously, a closer investigation indicates some small deviations, mostly at the early stages of the collapse particularly for small ϕ_i and small St (light grey squares). Assuming these deviations to be of second order, we focus here on the main curve holding all these trajectories.

The trend of the trajectory of the centre of mass can be predicted by deriving the trajectories of simple geometric models. In particular, according to the shapes observed for small spreading length situations and larger ones, one considers that the shape of the collapse remains either trapezoidal or triangular during the entire collapse. We obtain for the trapezoidal shape and the triangular shape, respectively,

$$\frac{2Y_g - H_i}{H_i} \sim - \left(\frac{2X_g - L_i}{L_i} \right)^{1/2} \quad \text{and} \quad \frac{2Y_g}{H_i} \sim \left(\frac{2X_g}{L_i} \right)^{-1}. \quad (3.1a,b)$$

These two solutions are plotted in figure 4 with dashed line and solid line, respectively. Such simple solutions are shown to predict quite well the numerical data far from the initial state, i.e. for $((2X_g - L_i)/L_i, (2Y_g - H_i)/H_i)$ sufficiently far from $(0, 0)$. In the latter case, the trapezoidal and triangular predictive models give an identical trend. However, closer to

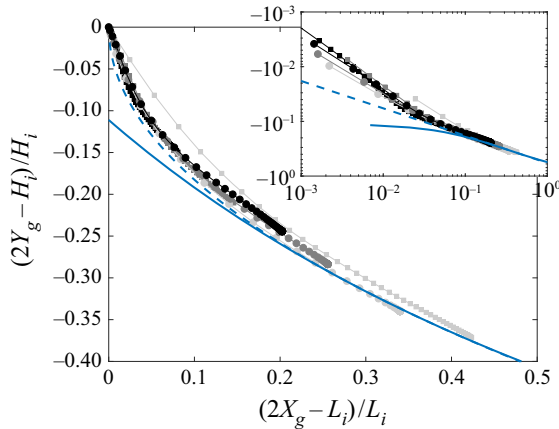


Figure 4. Trajectories of the dimensionless position of the centre of mass $((2Y_g - L_i)/L_i, (2X_g - L_i)/L_i)$ (inset: log–log representation). Light grey symbols, dark grey symbols and black symbols correspond to $\phi_i = 0.57$, $\phi_i = 0.59$ and $\phi_i = 0.63$, respectively (squares, $St = 6 \times 10^{-2}$, and circles, $St = 6 \times 10^{-1}$). Solid line (triangular shape) and dashed line (trapezoidal shape) correspond to model (3.1a,b).

the initial state, i.e. $((2X_g - L_i)/L_i, (2Y_g - H_i)/H_i) \approx (0, 0)$, the trapezoidal model gives a better estimation of the collapse evolution in the range of parameters considered here (dashed line). This is in accordance with the small aspect ratio $a = 0.5$ considered here, for which the granular medium remains in a trapezoidal shape during most of the collapse and particularly at the early stages, even if the final rest state can be closer to the triangular shape for some cases (small ϕ_i and small St , for instance). Note that it has been shown that situations with larger a are better estimated by the triangular model, as shown in Bougouin & Lacaze (2018) for laboratory experiments.

Even if these simple models give a first insight into the dynamics of the collapse, the final rest state remains unpredicted. In order to close model (3.1a,b), i.e. to predict the final state of the granular collapse, it would necessary to prescribe the time scale of the collapse and one of the final state morphological properties, such as the final spreading length or the final height or even the deposit slope. This is discussed in the next section.

3.3. Final-state morphology and time scale

In order to quantify the combined influence of (St, ϕ_i) on both the final state and the time scale of the collapse, figure 5(a–c), respectively, show the final run-out $r = (L_f - L_i)/L_i$, the mean deposit slope $\tan \alpha$ and the dimensionless collapse time scale T_{95}/T_c , as functions of St and for several ϕ_i ($\phi_i = 0.57$, green symbols; $\phi_i = 0.59$, red symbols; and $\phi_i = 0.63$, blue symbols). In figure 5(b), the mean deposit slope $\tan \alpha$ is defined as $\tan \alpha = L_f/H_f$ for a triangular deposit and as $\tan \alpha = (L_f - L_b)/H_f$ for a trapezoidal deposit (see inset of figure 5(b) for sketches and corresponding deposit lengths). Also shown in figure 5(b) is the maximum deposit slope $\tan \alpha_i$ obtained at the top of the deposit (dots). In figure 5(c), T_{95} corresponds to the time at which 95% of the final spreading length is reached by the front of the granular avalanche. Two different characteristic times T_c have been considered here (full symbols and open symbols in figure 5c) and defined as in Bougouin & Lacaze (2018). A so-called free-fall characteristic time $T_c = T_i = \sqrt{2\rho_p H_i / (\rho_p - \rho)g}$ corresponds to the time that a particle needs to fall from a height H_i with a constant acceleration induced by gravity g , assuming no interaction with the

Immersed granular collapse

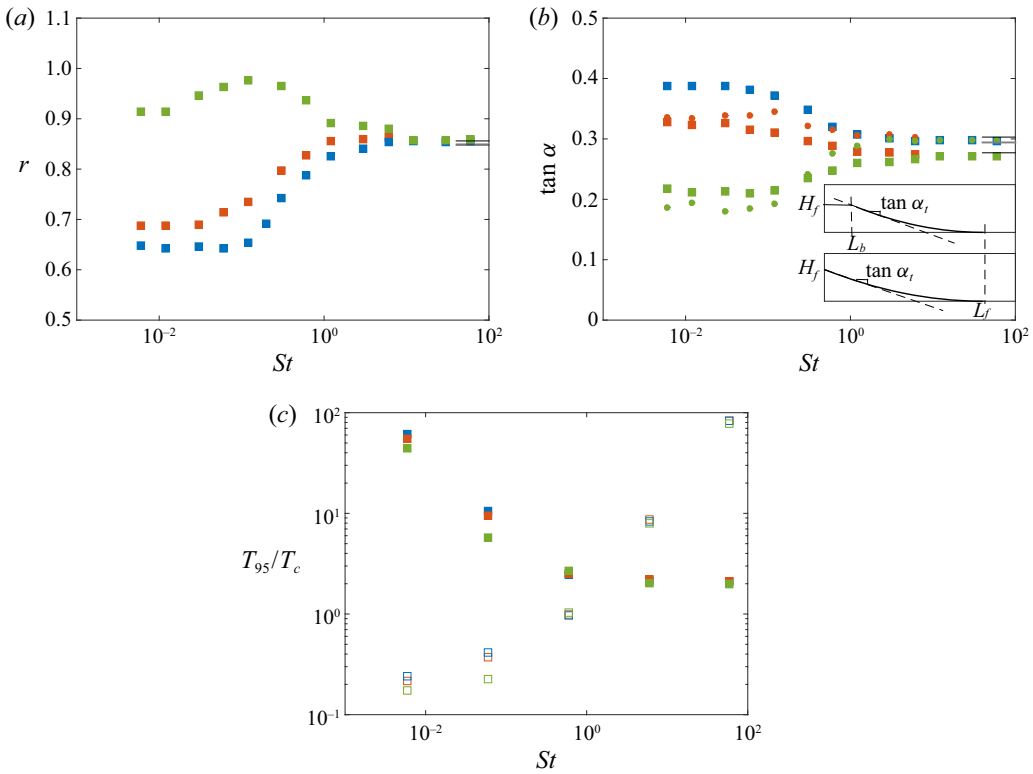


Figure 5. (a) Dimensionless run-out $r = (L_f - L_i)/L_i$, (b) mean deposit slope $\tan \alpha$ as defined in the text (squares) and maximum deposit slope $\tan \alpha_t$ (dots) as sketched in the inset and (c) dimensionless time scale T_{95}/T_c , all as a function of St (green symbols, $\phi_i = 0.57$; red symbols, $\phi_i = 0.59$; and blue symbols, $\phi_i = 0.63$). Full symbols in (c) correspond to $T_c = T_i$ while open symbols are for $T_c = T_v$ (see text for definitions of T_i and T_v). In (a,b), horizontal small black lines at large St correspond to dry simulations of the present configuration for $\phi_i = 0.57$ and $\phi_i = 0.63$, respectively, while dark grey lines are extracted from the experimental results of Lajeunesse *et al.* (2005).

surrounding fluid (full symbols in figure 5c). A second characteristic time corresponds to a viscous time scale that a grain needs to fall from a height H_i when its velocity remains constant as an equilibrium between weight and viscous drag. In this case, one can write $T_c = T_v = 18\eta H_i / (\rho_p - \rho)gd^2$ and the corresponding results are shown by empty symbols in figure 5(c).

When St is large enough, $St \geq 10$, figure 5(a) shows that $(L_f - L_i)/L_i$ is independent of ϕ_i and reaches the expected dry situation (grey horizontal line from experiments of Lajeunesse *et al.* (2005) and black horizontal lines from dry DEM simulations; dry DEM simulations are performed by removing the fluid solver on the same granular configuration). The spreading length then clearly decreases with decreasing St when the initial packing is dense enough, $\phi_i = 0.63$ and to a lesser extent $\phi_i = 0.59$, as could be expected from the role of viscous dissipation. Yet, the opposite trend is observed for the initial loose packing, $\phi_i = 0.57$. In particular, $(L_f - L_i)/L_i$ increases with decreasing St , reaching a maximum around $St = 0.12$. For $St < 0.12$, the spreading length slightly decreases with St as for the dense situations, but keeping a value larger than that for the large- St limit. For all ϕ_i reported here, $(L_f - L_i)/L_i$ reaches a plateau when $St \ll 1$, whose value increases for decreasing ϕ_i . Accordingly, figure 5(b) shows a similar trend for the deposit slope $\tan \alpha$ (squares). A noticeable difference, however, is observed at

large St , where a small difference in the deposit slope $\tan\alpha$ (as it is defined here) is obtained. This remains in the range of values reported from experiments (horizontal grey line from Lajeunesse *et al.* (2005)) and dry DEM simulations (horizontal black lines). This difference at large St quantifies the observations reported in figure 3(c,d), and is probably a signature of previous experimental observation on a similar configuration (Daerr & Douady 1999). Finally, the maximum slope close to the top of the deposit $\tan\alpha_t$ supports previous observations (dots in figure 5b). Small differences between $\tan\alpha_t$ and $\tan\alpha$ somehow measure an apparent uncertainty between the macroscopic behaviour induced by (St, ϕ_i) on the shape of the final deposit and a local manifestation of different spatio-temporal dynamics, close to the front or close to the upper part of the deposit. Then, accordingly, the influence of (St, ϕ_i) is considered as remaining small for $St \gtrsim 1.5$, above which $\tan\alpha_t$ no longer depends on St or ϕ_i .

At large St , the time scale of the collapse scales with a free-fall situation for which the fluid is disregarded (see full symbols in figure 5c). This time scale then strongly increases when St decreases (full symbols in figure 5c) to reach a viscous time scale whatever ϕ_i (open symbols in figure 5c). One observes here that the regime of the collapse, viscous versus free-fall, changes for $1 < St < 10$, actually close to $St \approx 1.5$, like the transition observed for the deposit shape mentioned previously. This confirms the influence of the viscous dissipation on the final deposit. Yet, fluid viscosity can act in a very different manner on the dynamics and the deposit when $St \rightarrow 0$, depending on the value of ϕ_i . A non-intuitive consequence is a possible enhancement of the spreading length due to the fluid viscosity. This means that the influence of the fluid viscosity is twofold: it not only slows down the collapse, as could be expected through St whatever ϕ_i , but also plays another role through ϕ_i at given St . The only other source of dissipation is obviously the granular friction, which has therefore to be strongly affected by ϕ_i . The rheological properties of the granular material then play a major role on these observations. This will be discussed in § 4.

3.4. *An effective St definition: unifying closure models and laboratory experiments*

Before discussing the rheological properties, we focus on the generalization of the above-mentioned results regarding the fluid phase closure models and with respect to experimental data available in the literature. So far, we have provided results for a given set of parameters of the closure models (2.6) and (2.8). According to the results discussed in the supplementary material, this specific set of parameters should contain all the required physics of the fluid phase at the microscale, smaller than d , to provide the expected behaviour of the collapse, at least qualitatively. This would mean that the influence of a specific choice of the closure model, in the range of that proposed in § 2.2, could only affect the dynamics quantitatively. We will show in this section that this quantitative influence of the closure models can actually be simply accounted for by defining an adequate effective Stokes number. Moreover, this will then be discussed in light of experimental results to highlight their predictability from the present simulations.

We have shown previously that the collapse is strongly affected by the transition from the viscous regime towards the free-fall regime. This transition has been shown to be controlled by the St number according to many configurations involving fluid–particle interactions. One can thus anticipate that closure models, affecting viscous dissipation at the microscale, should modify the critical range of St characterizing the transition from the viscous regime towards the free-fall regime. However, the qualitative trend obtained previously by varying (St, ϕ_i) should be maintained.

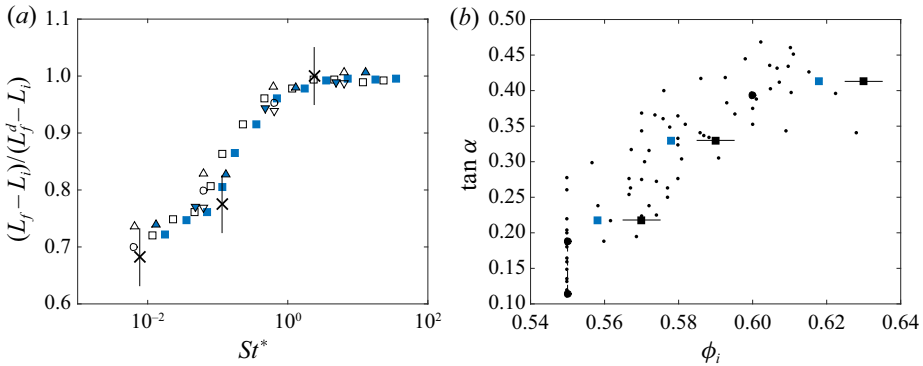


Figure 6. (a) Ratio of the spreading length $L_f - L_i$ to the dry one $L_f^d - L_i$ as a function of the effective Stokes number $St^* = St \times \eta/\eta_{eff}^M$ (open symbols) or $St^* = St/(\phi_i(1 - \phi_i)^{-\xi})$ (full symbols) for the initially dense configuration $\phi_i = 0.63$ (see text for details): simulations for ($\xi = 1, \eta_{eff}^M/\eta = 1 + 5\phi/2$) (squares) and an extra lubrication model (circles), ($\xi = 2, \eta_{eff}^M/\eta = 1 + 5\phi/2 + 7.6\phi^2 + 16\phi^3$) (upward-pointing triangle) and ($\xi = 3, \eta_{eff}^M/\eta = 1 + 5\phi/2 + 7.6\phi^2 + 16\phi^3$) (downward-pointing triangle); and experimental data from Bougouin & Lacaze (2018) (crosses with uncertainty). (b) Mean deposit slope $\tan \alpha$ as a function of ϕ_i : numerical simulations for ($\xi = 1, \eta_{eff}^M/\eta = 1 + 5\phi/2$) and $St \approx 6 \times 10^{-3}$ (black squares with uncertainty; blue squares correspond to the same simulations but shifting ϕ_i by ≈ 0.012 , a value based on the difference of rheological parameters between experiments and simulations, as explained in §4.1), experimental data from Rondon *et al.* (2011) for $St \approx 5 \times 10^{-2}$ (small dots) and for $St \approx 5 \times 10^{-2}$ and $a \approx 0.5$ or $a \approx 0.65$ (big dots).

To highlight that assumption, different models have been considered for $\phi_i = 0.63$ and varying St . The results are reported in figure 6(a). The different symbols correspond to different closure models, namely ($\xi = 1, \eta_{eff}^M/\eta = 1 + 5\phi/2$) (squares; circles correspond to the same closure models but with an extra lubrication force added into the DEM contact model as in Izard *et al.* (2014)), ($\xi = 2, \eta_{eff}^M/\eta = 1 + 5\phi/2 + 7.6\phi^2 + 16\phi^3$) (upward-pointing triangles), and ($\xi = 3, \eta_{eff}^M/\eta = 1 + 5\phi/2 + 7.6\phi^2 + 16\phi^3$) (downward-pointing triangles). One shows in this figure that providing a relevant definition of St , say St^* , allows the different cases almost to collapse onto a master curve. In particular, this modification of St includes the influence of ϕ_i through the effective models as $St^* = St \times \eta/\eta_{eff}^M$ (open symbols in figure 6a) or $St^* = St/(\phi_i(1 - \phi_i)^{-\xi})$ (full symbols in figure 6a), i.e. accounting for the ϕ_i contribution included in either the effective viscosity closure model or the effective drag closure model, respectively. Note that, for the specific situation of an additional lubrication force in the contact model (circles), the definition of St^* chosen as $St^* = St\eta/\eta_{eff}^M$ uses $\eta_{eff}^M/\eta = 1 + 5\phi/2 + 7.6\phi^2 + 16\phi^3$, even if the first-order Einstein viscosity was used here, as lubrication adds dissipation, which is not incorporated in the fluid phase solver. Then, one shows that models used for drag and/or viscosity, and even lubrication, only shift the transition from viscous to free-fall regimes, which could be easily understood using an appropriate definition of the St number. This is a remarkable result, as it provides the relevance of the mesoscale approach for modelling immersed granular flows, even if the accurate closure models to be used are still debated.

A comparison of the results with available experimental data is given in figure 6. More particularly, figure 6(a) compares the influence of St in a dense configuration $\phi_i \approx 0.64$ on the spreading length as experimentally studied by Bougouin & Lacaze (2018), and

figure 6(b) shows the comparison of the deposit angle as a function of ϕ_i at small St as reported by Rondon *et al.* (2011). In figure 6(a), the final spreading length is shown relative to the dry one. This is done to ensure comparability between the numerical simulations and the experiments, for which the bottom surface is different. In figure 6(b), the comparison is done on the deposit slope $\tan \alpha$. Moreover, note that, here, the values of St between numerical simulations and experiments are slightly different. However, their small values ensure a viscous regime, for which the final state remains roughly unchanged up to $St \approx 10^{-1}$. In both cases (figure 6a,b), a good agreement is obtained between the numerical simulations and the experimental data. In particular, the evolution of the final deposit as a function of (St, ϕ_i) is clearly captured and, moreover, the quantitative ranges of evolution are in reasonable agreement. Note that, as the value of ϕ_i is very sensitive, we also provide in figure 6(b) results for which ϕ_i is slightly shifted for the numerical data (blue squares; the shift value is not arbitrary and is based on the difference of equilibrium rheological states obtained in experiments and simulations as explained in § 4).

It can be noted that adding ϕ_i in St^* only accounts for the rate of fluid dissipation induced by compaction in the granular pores. This allows one to capture the relevant range of variation of the final state as a function of fluid dissipation (figure 6a) but not to provide, solely, an explanation for the influence of ϕ_i at given St reported in the previous section. In fact, the latter highlights a too significant influence on the final state to be attributed only to the definition of St^* . This shows again that the obtained results are to be linked to a significant influence of the rheological properties of the granular phase.

4. Rheological model of the granular phase

Following Lacaze & Kerswell (2009), we use here a coarse-graining approach to extract the equivalent stress tensor of the granular medium in this unsteady configuration. We do not recall this methodology here, as it has become quite standard, and we simply refer the reader to Goldhirsch & Goldenberg (2002) for details. It should be noted that the granular collapse is an interesting configuration to test and validate rheological models – as equilibrium models obtained from steady and one-dimensional shear flows – in the case of unsteady and multi-directional shear configurations. Moreover, it allows one to extract out-of-equilibrium local behaviours, which could be significant for unsteady configurations and required to improve models. In return, the averaging procedure of the coarse-graining method has to be localized in space and time to extract the local component of the shear and stress tensors, which are space- and time-dependent (Lacaze & Kerswell 2009). This usually leads to relatively dispersed results, as will be shown in the following. Note, however, that the granular collapse allows one to cover a wide range of dynamical properties such as shear rate and stress contribution, allowing most of the rheological law to be extracted, during a single event.

Here, coarse graining is performed on a regular grid in the (x, y) plane of resolution $2d$ at different times of the collapse. The averaging procedure is performed over volumes of Gaussian shape in (x, y) of standard deviation d and invariant in the z direction. From the coarse-grained results, the rheological law will be characterized by the local volume fraction ϕ , which can also be referred to the local state of the granular material, and the coefficient of local effective friction μ defined as

$$\mu = \|\langle \boldsymbol{\tau} \rangle_p\| / \langle p \rangle_p, \quad (4.1)$$

with both the deviatoric contribution of the granular stress tensor $\langle \boldsymbol{\tau} \rangle_p$ and the granular pressure $\langle p \rangle_p$ being obtained from the coarse-graining method. Once again, in such a

configuration, all these quantities depend on (x, y) and t . In the case of a 3-D flow, $\|\cdot\|$ refers to the second invariant of a tensor.

The $\mu(I)$ rheology as defined in Jop, Forterre & Pouliquen (2006) is used as the relevant rheological model, but including the extension of Trulsson *et al.* (2012) defined when transition from viscous to free-fall granular flow occurs, as observed, for instance, when increasing St (see previous section). Note that, in gravity-driven configuration, a distinction is sometimes made between inertial and free-fall regimes, for which ‘inertial’ is referred to as the state of the fluid drag at large Re_p . However, Bougouin & Lacaze (2018) shows that a fluid-inertial regime that would differ from the free-fall regime is hardly observable in the range of properties of the immersed granular collapse covered here. Thus, we do not clearly distinguish the inertial regime and the free-fall regime, as they both share quite common features for the granular phase. In Trulsson *et al.* (2012), the high- St limit is referred to as an inertial regime in their neutrally buoyant configuration. However, inertial refers to the inertia of the grain and the rheology then shares the same features as for the dry situation. This is basically the same as the free-fall case considered here, in which gravity now drives particle inertia through their apparent weight, i.e. weight and buoyancy.

The rheological model defines the effective friction μ of the granular material as a function of a single dimensionless number, comparing a time scale of macroscopic deformation of the granular media induced by a shear $\|\langle \dot{\gamma} \rangle_p\|$ and a microscopic time scale of rearrangement of the media due to a confining granular pressure $\langle p \rangle_p$. Depending on the flow regime, Cassar *et al.* (2005) have proposed two different relevant definitions for this dimensionless number, say J in the viscous regime and I in the free-fall regime. Trulsson *et al.* (2012) then proposed a combination of these different definitions I and J , labelled K , unifying a large range of St , from the viscous regime to the free-fall regime.

One therefore uses the dimensionless number K , which can be written as

$$K = J + \beta I^2, \quad \text{with} \quad \begin{cases} J = \frac{\eta \|\langle \dot{\gamma} \rangle_p\|}{\langle p \rangle_p}, \\ I = \frac{\|\langle \dot{\gamma} \rangle_p\| d}{\sqrt{\langle p \rangle_p / \rho_p}}, \end{cases} \quad (4.2)$$

where β is a constant, found to be ≈ 0.65 in Trulsson *et al.* (2012). It should be noted that this value of β was found for 2-D simulations. In the present case of 3-D simulations, a different value could be obtained. However, in the range of parameters considered here, small variations of β around this reference value do not show any significant improvement for universal collapse of the rheological data. It has been chosen to be set to the value already proposed by Trulsson *et al.* (2012). Note that dedicated 3-D simulations should help in adjusting this parameter more accurately for 3-D configurations.

4.1. Influence of St in the loose packing configuration

In this section, we focus on the initial loose packing configuration, i.e. $\phi_i = 0.57$. This initial case is first considered as most of the initial column contributes to the granular motion, while for large ϕ_i , most of the bottom-left corner remains static during the collapse. It will be shown that this configuration more clearly highlights an equilibrium state according to the rheological and state parameters (ϕ, μ) , as obtained in steady flows.

The discussion on the rheological results obtained from the coarsening method is first discussed over the entire collapse without making any distinction between specific regions, i.e. over the domain $\mathcal{A} \in \{x > 2d, y > 2d, y < h(x, t)\}$, with h the time-dependent height profile of the granular medium, and over a linear time-stepping scale, as $t \in [0, T_{95}]$ with a

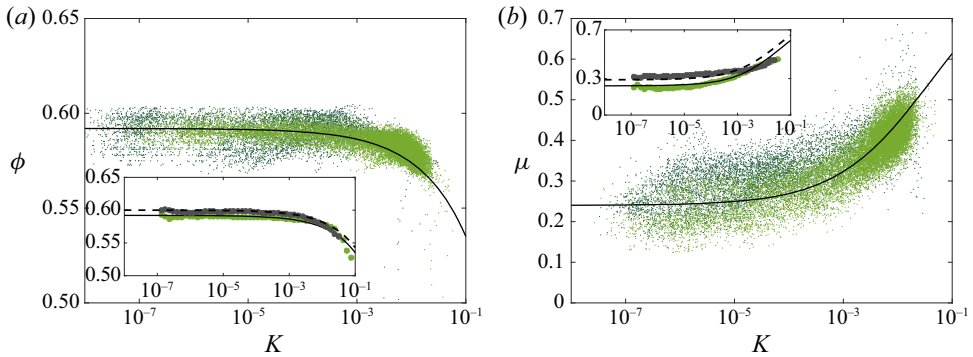


Figure 7. (a) Volume fraction ϕ and (b) effective coefficient of friction μ as functions of K for $(St, \phi_i) = (6 \times 10^{-3}, 0.57)$ (light green dots) and $(St, \phi_i) = (6, 0.57)$ (dark green dots). Inset: average data on a regular K scale from rough local data. Solid lines correspond to model (4.3) with $\phi_c = 0.592$, $a = 0.18$, $\mu_c = 0.24$, $\Delta\mu = 0.6$ and $\sqrt{K_0} = 0.2$. Dashed lines correspond to the model used at large St and extracted from figure 8(b), i.e. $\phi_c = 0.6$ and $\mu_c = 0.29$, keeping the other parameters equal to the former case.

time step $T_{95}/10$. Note that T_{95} is a function of St ; thus this time stepping accounts for the different dynamics of the collapse to cover regularly the full range of evolution. Moreover, boundaries are excluded from the analysis, as they would need a specific attention such as an adapted coarse-graining approach (Weinhart *et al.* 2012).

Only the influence of St is thus considered here. The results obtained from the coarse-graining approach are shown for $(St, \phi_i) = (6 \times 10^{-3}, 0.57)$ (light green symbols) and $(St, \phi_i) = (6, 0.57)$ (dark green symbols) in figure 7. Note that larger values of St have been performed up to $St = 60$, for which no significant difference is observed from $St = 6$. Thus $St = 6$ is discussed here without altering the analysis. The volume fraction ϕ and the effective friction μ are plotted as functions of K in figures 7(a) and 7(b), respectively. We can first note that, beyond an important dispersion of the results as anticipated, ϕ and μ show a clear evolution with respect to K , thus highlighting the relevance of the parameter K as the controlling dimensionless parameter to describe the rheology of immersed granular material. Moreover, the two different cases $(St, \phi_i) = (6 \times 10^{-3}, 0.57)$ and $(St, \phi_i) = (6, 0.57)$ nearly collapse onto a similar trend curve, even if a slight difference is actually observed, as will be discussed in the following. These observations reinforce the role of K , whose purpose is to unify the different regimes from viscous to free-fall.

The results obtained here show that, at small ϕ_i , the rheology is not significantly affected by St , and that the obtained critical volume fraction $\phi_c = \phi(K \rightarrow 0)$ is larger than that in the initial state. These observations suggest that the rheological state is close to a somehow universal one, independent of the initial state, which should therefore be expected to be the one obtained for steady-state systems. We thus compare these results to the model proposed by Trulsson *et al.* (2012) obtained for steady state and considered here as the equilibrium state rheology. This model can be written as

$$\left. \begin{aligned} \phi_{eq} &= \phi_c - a\sqrt{K}, \\ \mu_{eq} &= \mu_c + \frac{\Delta\mu}{\sqrt{K_0/K} + 1}, \end{aligned} \right\} \quad (4.3)$$

where subscript *eq* stands for equilibrium. In figure 7, black solid lines correspond to the model (4.3) with $\phi_c = 0.592$, $a = 0.18$, $\mu_c = 0.24$, $\Delta\mu = 0.6$ and $\sqrt{K_0} = 0.2$.

Immersed granular collapse

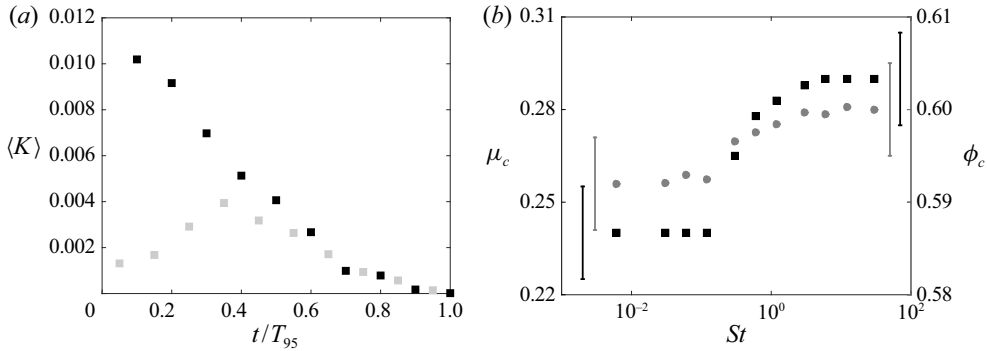


Figure 8. (a) Evolution of $\langle K \rangle$ as a function of time t/T_{95} over the domain \mathcal{A}_D (see text for details) for $(St, \phi_i) = (6 \times 10^{-3}, 0.57)$ (black squares) and $(St, \phi_i) = (6, 0.57)$ (grey squares). (b) Plot of μ_c (black squares) and ϕ_c (grey circles) as functions of St . Vertical lines in (b) indicate the typical uncertainty in evaluating μ_c and ϕ_c .

These values correspond to the best fit that can be obtained from the data shown in [figure 7](#) for $St = 6 \times 10^{-3}$, which shows less dispersion. Moreover, the values for $\Delta\mu$ and $\sqrt{\langle K \rangle_0}$ are consistent with results obtained for the dry collapse (Lacaze & Kerswell 2009). This leads to values of the fitting data that are in reasonable agreement with what is obtained in the literature. It can also be noted at this point that the usual value of ϕ_c found in experiments is around 0.58 (see, for instance, Pailha & Pouliquen 2009). The ≈ 0.012 difference of ϕ_c between experiments and simulations has thus been used as the shift value for ϕ_i in [figure 6\(b\)](#) (blue symbols).

The agreement between numerical results and the equilibrium model in [figure 7](#) confirms the reliability of this model in the case of an unsteady and 3-D configuration for a large range of St , at least for $\phi_i = 0.57$. However, a closer inspection of the results suggests that the influence of St is not non-existent, and that the spatio-temporal domain of extraction of the rheological characteristics requires specific attention, as it highlights different states during collapse. This point is discussed in the following, and will also be considered attentively in the next section.

As mentioned above, the general rheological trend given in [figure 7](#) is obtained at 10 regularly spaced time steps for $t \in [0, T_{95}]$. At large St , this includes both accelerating and decelerating stages of the collapse, while at small St it only includes decelerating stages. This is highlighted in [figure 8\(a\)](#) in which the average value $\langle K \rangle$ is plotted as a function of t/T_{95} for $St = 6 \times 10^{-3}$ and $St = 6$, and with $\langle K \rangle$ being the spatial average of K over the non-static area $\mathcal{A}_D \in \{x > 2d, y > h_s(x), y < h(x, t)\}$, where h_s is the height profile delimiting the granular region which remains static for $t \in [0, T_{95}]$.

We now focus on the decelerating stage, referred to as the resting stage, which is characterized as the time interval of decreasing $\langle K \rangle$. Note that, according to the results shown in [figure 8\(a\)](#), the case $St = 6 \times 10^{-3}$ is not significantly affected by this new procedure, as previous results were already obtained in the resting stage. However, this is somehow different for $St = 6$, for which part of the coarse-grained results are removed with this new procedure. It explains the more important dispersion of results for $St = 6$ in [figure 7](#). Using this new procedure, each St is investigated independently. The insets of [figure 7](#) show the average values of ϕ and μ , respectively, obtained on \mathcal{A}_D during the resting stage, for the two values of St considered previously. The average is obtained here by binning the spatio-temporal rough data in log-scale compartments of K .

This first confirms the K trend of both ϕ and μ . Moreover, μ and ϕ merge at large K for the different St , typically $K > 10^{-3}$ here, i.e. at the beginning of the resting stage. This would naturally support the fact that the granular material has reached a universal equilibrium state. However, according to the definitions of ϕ_c and μ_c in (4.3) and obtained as $K \rightarrow 0$ during the resting stage, this refined investigation shows that they are both functions of St . The dependences of ϕ_c and μ_c with St are shown in figure 8(b).

The evolution of $\mu_c(St)$ and $\phi_c(St)$ shown in figure 8(b) highlights a rapid transition around $St \approx 1$ delimiting two asymptotic behaviours at small St and large St , at which plateaus are obtained. In particular, for both μ_c and ϕ_c , the values on these plateaus are found to be slightly larger for $St \gg 1$ than for $St \ll 1$. Note that the value found at $St \gg 1$ is very close to that reported for dry collapses in Lacaze & Kerswell (2009). However, the physical reason for the sudden decrease of μ_c at small St remains unclear, even if viscous/free-fall transitions are usual observations for several properties in different configurations (see, for instance, Gondret, Lance & Petit (2002) for the case of particle bouncing). It can be at least noted that this is associated with the state of the granular medium for $K \rightarrow 0$, as ϕ_c follows a similar trend, such that μ_c decreases with ϕ_c . This indicates an influence of the history of the collapse on the final state, through St , which leads to a small deviation from a universal equilibrium law.

For an unsteady configuration such as collapse, the state of the granular system and its associated rheological law, described here by ϕ and μ during the resting stage, i.e. for decreasing K , are close to the equilibrium law obtained for steady flows. However, the unique function of K with constant parameters in (4.3) as obtained in steady configurations is not clear in the state. Here, different states can exist for the same value of K . In the loose configuration considered here, it has been shown to be possibly modelled by including a St dependence in μ_c and ϕ_c , keeping the trend of the equilibrium model. To finish with, note that the obtained evolution of $\mu_c(St)$ is in line with the conclusions drawn previously from the final state shape of the initial loose packing case, i.e. the spreading length increases while μ_c decreases for decreasing St (see figure 5b).

4.2. Influence of ϕ_i at small St

The same procedure can be followed to identify the influence of the initial volume fraction ϕ_i . As the influence of ϕ_i is clearer at small St , we focus here on $St = 6 \times 10^{-3}$. In this case, the granular flow remains in the viscous regime and then $K = J$. Figure 9 reports the coarse-graining results obtained over the temporal interval $t \in [0, T_{95}]$ with a time step $T_{95}/10$ and over the spatial domain $\mathcal{A} \in \{x > 2d, y > 2d, y < h(x, t)\}$, as done in the previous section. More particularly, the volume fraction ϕ and the effective coefficient of friction μ are plotted as functions of J for $(St, \phi_i) = (6 \times 10^{-3}, 0.57)$ (green symbols) and $(St, \phi_i) = (6 \times 10^{-3}, 0.63)$ (blue symbols) in figures 9(a) and 9(b), respectively. Note, again, that the equilibrium law is recovered for $\phi_i = 0.57$ on this spatio-temporal domain, as discussed in the previous section. Yet, as observed in figure 9, the case $\phi_i = 0.63$ does not show the same trend as for $\phi_i = 0.57$; the influence of the initial decompaction of the granular medium prior to collapsing cannot be disregarded from the rheological point of view. This behaviour has been reported in Pailha & Pouliquen (2009), specifying a dilatancy angle ψ having to be accounted for when defining the effective friction angle. Following their analysis, we define the dilatancy angle ψ as

$$\tan \psi = \nabla \cdot \langle \mathbf{v} \rangle_p. \tag{4.4}$$

Immersed granular collapse

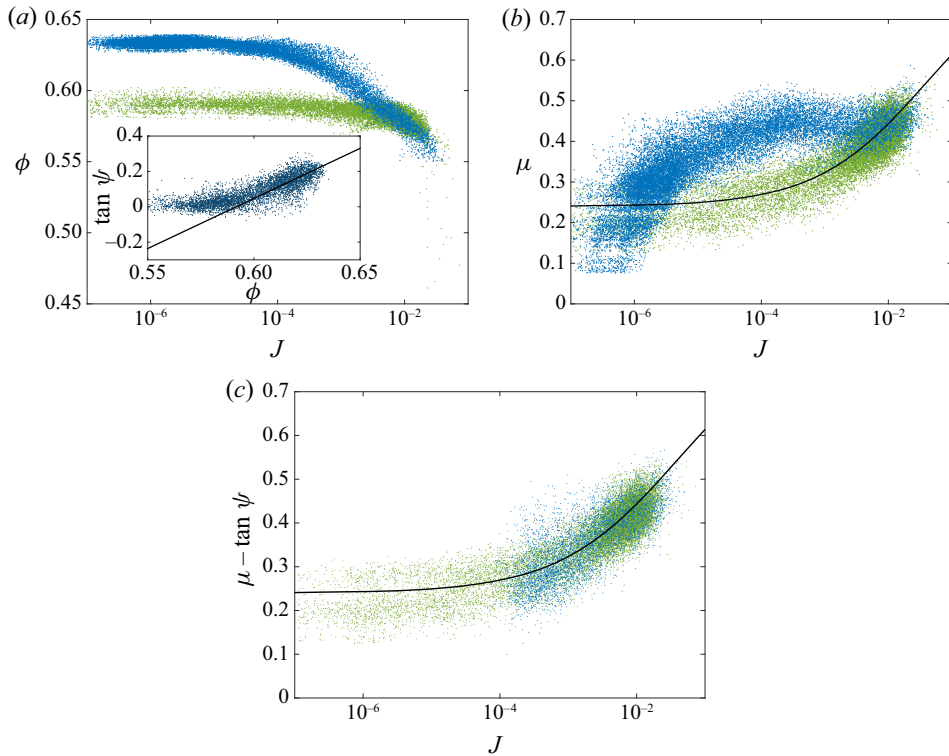


Figure 9. (a) Volume fraction ϕ and (b) effective coefficient of friction μ as functions of J for $(St, \phi_i) = (6 \times 10^{-3}, 0.57)$ (green dots) and $(St, \phi_i) = (6 \times 10^{-3}, 0.63)$ (blue dots). Inset of (a): Angle of dilatation $\tan \psi$ (4.4) as a function of ϕ for $(St, \phi_i) = (6 \times 10^{-3}, 0.63)$. (c) Corrected coefficient of friction $\mu - \tan \psi$ as a function of J (symbols are similar to panels a,b). Note that the dilatation effect for $\phi_i = 0.57$ is hardly observable, so its correction $\tan \psi$ has therefore been neglected for this case (green dots in c); and the dilatation angle correction $\tan \psi$ is only observable when grain motion is significant enough, so data below $J \approx 10^{-4}$, i.e. in the plastic region, have therefore been disregarded for $\phi_i = 0.63$ (blue dots in c). Solid lines in (a,c) correspond to model (4.5) with $\phi_{eq} = \phi_c$. Solid line in (b) corresponds to model (4.3).

The rheological model (4.3) can then be modified to include the influence of the dilatancy angle ψ as discussed in Roux & Radjai (1998) and Pailha & Pouliquen (2009),

$$\left. \begin{aligned} \tan \psi &= b(\phi_{oeq} - \phi_{eq}), \\ \mu_{oeq} - \tan \psi &= \mu_c + \frac{\Delta \mu}{\sqrt{K_0/J + 1}}, \end{aligned} \right\} \quad (4.5)$$

where subscript *oeq* stands for out of equilibrium. According to this model, $\mu - \tan \psi$ is plotted as a function of J in figure 9(c), with the same symbols as previously. For $\phi = 0.63$, only values above $J \approx 10^{-4}$ are reported here. As will be shown later, this is actually similar to considering only the moving region of the granular medium after the initial stages of the collapse corresponding to the initial expansion of the granular material. Below $J \approx 10^{-4}$, the $\mu - \tan \psi$ does not collapse on the same curve (not shown here). The reason can probably be attributed to the connection with the plastic region, which is not well captured by the $\mu(J)$ rheology (probably related to the behaviour of the $\mu(I)$ rheology at small I as discussed in Barker & Gray (2017)). This very specific behaviour should be addressed in future works but is beyond the scope of the present paper, as it does not

significantly affect the physics and the dynamics of the collapse. However, for $J > 10^{-4}$, one obtains a collapse of $\mu - \tan \psi$ onto a single function of J for $\phi_i = 0.57$ and $\phi = 0.63$.

In order to predict simply the rheological behaviour shown in figure 9, we can first assume that $\phi_{eq} \approx \phi_c$ in (4.5), as it is shown to be roughly constant in the inset of figure 9(a), where $\tan \psi$ is shown to be a single linear function of ϕ whatever J . This is, moreover, shown here to be equal to $\phi_c = 0.592$ (intersection of the solid line and $\tan \psi = 0$ in the inset of figure 9(a), similar to the value obtained with model (4.3) for $(St, \phi_i) = (6 \times 10^{-3}, 0.57)$. The solid lines in figure 9(a,c) correspond to the model (4.5) with $\phi_{eq} = \phi_c$ keeping the values of μ_c , $\Delta\mu$ and K_0 obtained previously and $b = 5.5$. This model prescribes relatively well the trends of rheological parameters obtained from the simulations, particularly for $\mu - \tan \psi$ as a function of J and $\tan \psi$ as a function of ϕ , highlighting the influence of the deviation of the volume fraction ϕ with respect to a reference value ϕ_c . Nevertheless, this model does not allow the trend of ϕ_{oeq} as a function of J to be provided, i.e. model (4.5) is not closed as we basically end up with one equation for two unknowns (ϕ_{oeq}, μ_{oeq}).

A slightly more advanced approach to close the rheological model (4.5) in our configuration would be to prescribe ϕ_{oeq} . This is not necessarily an obvious task without solving an appropriate time-dependent equation. For the sake of simplicity, we propose in the following a prediction based on the expected behaviour of ϕ_{oeq} , or more likely of $\tan \psi$, during the collapse. For that purpose, we rewrite the dilatancy angle ψ such that

$$\tan \psi = -\frac{1}{\phi} \frac{D\phi}{Dt} \dot{\gamma}^{-1} = -\frac{1}{\phi} \frac{D\phi}{D\tilde{t}} J^{-1}, \tag{4.6}$$

where $\tilde{t} = t/t_m$ with $t_m = \eta/\langle p \rangle_p$ is a microscopic time scale of rearrangement of the granular material in the viscous regime (Cassar *et al.* 2005). As dilatation/compaction are precisely a rearrangement process, then we can assume that $(1/\phi)D\phi/D\tilde{t} = O(1)$ and then $\tan \psi \sim J^{-1}$. That said, we seek a solution that is also regular when $J \rightarrow 0$. As shown in figure 9(a), $\phi(J \rightarrow 0)$ can take several values. However, these values can be anticipated to be either ϕ_i or ϕ_c , depending on the situation. These situations can be distinguished, as $J \rightarrow 0$ at two different stages of the collapse, say at the very beginning of the collapse and when reaching its final rest state. In particular, the former case $\phi(J \rightarrow 0) = \phi_i$ is more likely to be expected at the initial stage of the collapse, when the granular medium starts from an imposed volume fraction ϕ_i . This will be referred to as the initiation stage. The latter case, $\phi(J \rightarrow 0) = \phi_c$, on the other hand, is more likely to be reached at the end of the collapse when the granular material returns to rest. As already discussed in the previous section, this resting stage could be considered as mainly described by its equilibrium state. This can be summarized as $\phi(J \rightarrow 0, t \rightarrow \{0; t_f\}) = \{\phi_i; \phi_c\}$. A solution that would be consistent with (4.5) and (4.3) when $J \rightarrow 0$ should then have the form $\tan \psi \rightarrow b(\phi_i - \phi_c)$ for an initiation state and $\tan \psi \rightarrow b(\phi_c - \phi_c) = 0$ for a resting state.

We thus propose the following simple model that would account for the out-of-equilibrium state during the granular collapse:

$$\left. \begin{aligned} \phi_{oeq} &= \phi_{eq} + \frac{(\{\phi_i; \phi_c\} - \phi_c) J_1}{J + J_1}, \\ \mu_{oeq} &= \mu_{eq} + \frac{b(\{\phi_i; \phi_c\} - \phi_c) J_1}{J + J_1}, \end{aligned} \right\} \tag{4.7}$$

where $\{\phi_i; \phi_c\}$ takes one of these values depending on the considered stage, i.e. initiation versus resting. Note, again, that, with this description, the resting stage is nothing but

an equilibrium state. In (4.7) J_1 is a regularization term allowing one to reach a finite non-zero value when $J \rightarrow 0$. Its value is found here to be $J_1 \approx 10^{-3}$ to fit the numerical data. This can be seen as the transition from the dominance of the dilatation/compaction effect towards a rheology controlled by the equilibrium state, this transition being found here to be controlled by the number J .

In order to show the relevance of the above-mentioned model, one proposes in the following to extract and to separate results from simulations during the so-called initiation stage and resting stage, labelled in the following as (.i) and (.ii), respectively. For that purpose, the distinction between these two stages has to be prescribed. We propose here to use the temporal evolution of averaged quantities over the granular medium. We thus plot the evolution of $\langle J \rangle$ and $\langle \phi \rangle$ as a function of t/T_v in figure 10(a,b) for both $\phi_i = 0.57$ (left column, labelled L for loose) and $\phi_i = 0.63$ (right column, labelled D for dense). Recall that T_v is a viscous time scale. Here, the procedure to obtain $\langle \cdot \rangle$ is the same as that explained in § 4.1 but over the domain $\mathcal{A}_{Dt} \in \{x > 2d, y > h_s(x, t), y < h(x, t)\}$, with h_s delimiting the flowing region and plastic region at each time step. Note that domain \mathcal{A}_{Dt} is slightly more restrictive than \mathcal{A}_D as used previously in § 4.1.

For the loose packing configuration L , one observes that the dynamics of the collapse, measured as $\langle J \rangle$, quickly reaches its maximum inertial state, and then $\langle J \rangle \rightarrow 0$. At the same time $\langle \phi \rangle$ increases during all the collapse (see figure 10a). However, in the log-linear representation of figure 10(a), the slope of $\langle \phi \rangle(t/T_v)$ suddenly changes. This also corresponds to a change in slope of $\langle J \rangle(t/T_v)$. This time is chosen as a delimitation of region (L.i) and region (L.ii). For the dense packing configuration, the evolutions of $\langle J \rangle$ and $\langle \phi \rangle$ are slightly different (see figure 10b). In particular, a first initial stage (D.0) is observed during which $\langle J \rangle \approx 0$. This corresponds to the initial dilatancy during which both $\langle J \rangle$ and $\langle \phi \rangle$ evolve very slowly. Then $\langle J \rangle$ increases suddenly. The rest of the dynamics can also be separated into two stages (D.i) and (D.ii) roughly similarly to the loose configuration, and therefore corresponding to the initiation stage and resting stage. Here, however, the delimitation is characterized by an inversion of evolution of $\langle \phi \rangle(t/T_v)$ which decreases during (D.i) and increases during (D.ii). Note that, in both cases (loose and dense), the chosen delimitation between stages (.i) and (.ii) more clearly corresponds to a change in the evolution of the state of the granular medium through the evolution of $\langle \phi \rangle$. However, it is clear from figure 10(a,b) that this separation also delineates dynamical stages of the collapse, as for instance $\langle J \rangle$ is maximum during the initiation stage (.i), while it slowly goes to zero during the resting stage (.ii). On the other hand, stages (.i) and (.ii) actually correspond to significant difference in the mass evolution, and thus the run-out, between loose and dense configurations (as shown by the snapshot of the grains' positions in figure 10a,b; black dots correspond to moving grains). In particular, T_{95} is obtained at the end of stage (L.ii) for the loose configuration, while it is at the end of (D.i) or only early (D.ii) for the dense one. Note that the latter observation explains the coarse-grained results shown in figure 9, as will be discussed later.

Using the above-mentioned delimitation in time, the rheological and state variables μ and ϕ are plotted as a function of J during stage (.i) (red dots) and stage (.ii) (green dots) in figure 10(c,d). Here, coarse-graining is performed over the spatial domain \mathcal{A}_{Dt} . Even though coarse-grained results are a bit sparse, trends can be observed. These coarse-grained results are compared to the model (4.7) for $\phi(J \rightarrow 0, t \rightarrow 0) = \phi_i$ (solid line) and $\phi(J \rightarrow 0, t \rightarrow t_f) = \phi_c$ (dashed lines). The qualitative agreement between the model and the simulations confirms the assumptions used to obtain model (4.7).

To finish, we come back to the results obtained in figure 9. Recall that, there, coarse-grained results were obtained in the interval $t \in [0, T_{95}]$ over a regular time grid

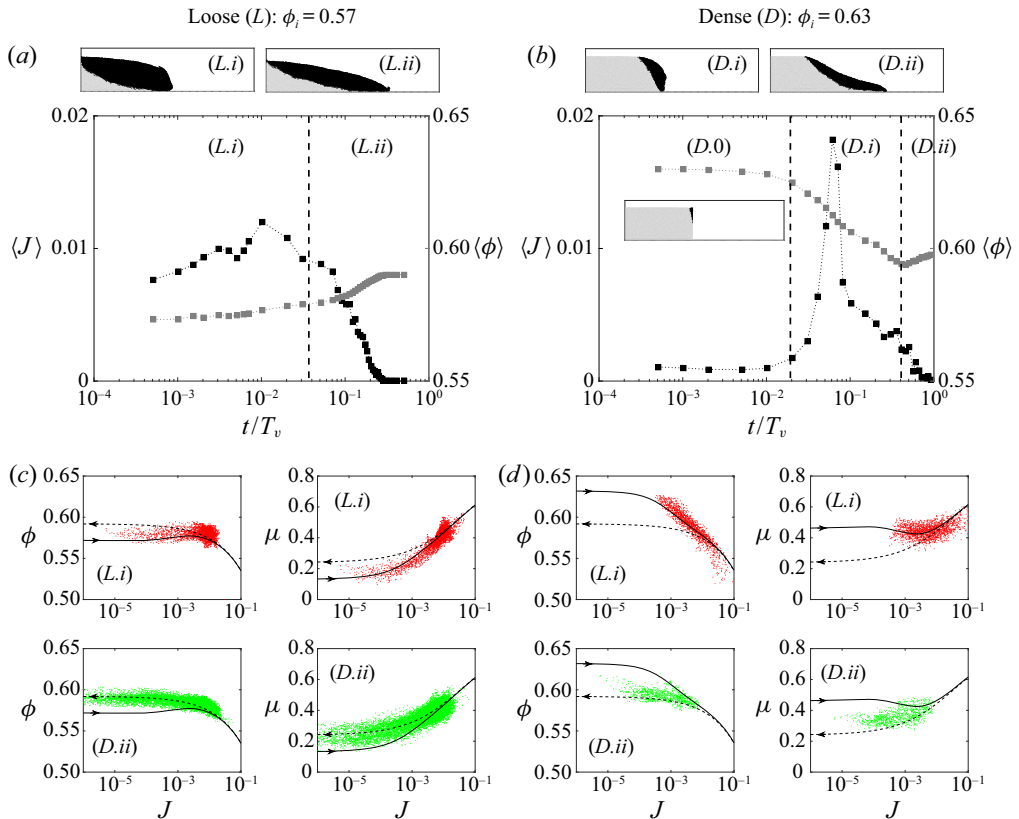


Figure 10. Time-dependent rheology of the viscous collapse, $St = 6 \times 10^{-3}$, for $\phi_i = 0.57$ (loose L , left column) and $\phi_i = 0.63$ (dense D , right column). (a,b) Plots of $\langle J \rangle$ (black symbols) and $\langle \phi \rangle$ (grey symbols), averaged over domain \mathcal{A}_{Dt} (see text for details), as a function of time (upper plots show snapshots of the granular medium within the different phases with static grains in grey and moving grains in black). (c,d) State and rheological parameters ϕ and μ as functions of J for the different phases as labelled in each panel. In all panels, (.0), (.i) and (.ii) correspond to the different stages of the granular flow according to its dynamical behaviour and rheological state: (.0) is an initial decompaction stage prior to collapsing only observed for dense configuration (D .); (.i) corresponds to the initiation stage as an accelerating phase of the collapse; and (.ii) is the resting stage during which the granular material goes to rest.

in a linear scale, and also includes the static region. According to results reported in figure 10 and the scale of T_{95} for the loose and dense configurations, the spreading phase $t \in [0, T_{95}]$ mostly lasts at the end of ($L.i$) and during ($L.ii$) for the loose configuration, while it mostly lasts during ($D.i$) for the dense one. In figure 11, one compares model (4.7) with this previously obtained coarse-grained results. The solutions of (4.7) are shown here for $\{\phi_i; \phi_c\} = \phi_i = [0.57 : 0.01 : 0.63]$ (thin lines), with highlights on $\{\phi_i; \phi_c\} = \phi_c$ (dashed line) and $\{\phi_i; \phi_c\} = \phi_i = 0.63$ (solid line). We can first conclude that the model proposed is in good agreement with numerical data showing its relevance for out-of-equilibrium situations. Moreover, the dense packing configuration highlights more clearly an out-of-equilibrium law model with $\{\phi_i; \phi_c\} = \phi_i$ while the loose packing situation shows an equilibrium state, i.e. $\{\phi_i; \phi_c\} = \phi_c$, during most of the spreading phase $t \in [0, T_{95}]$. This latter remark does not mean that the loose configuration is not affected by the initiation stage, but that it happens on a short time scale compared to the entire collapse one, unlike the dense configuration.

Immersed granular collapse

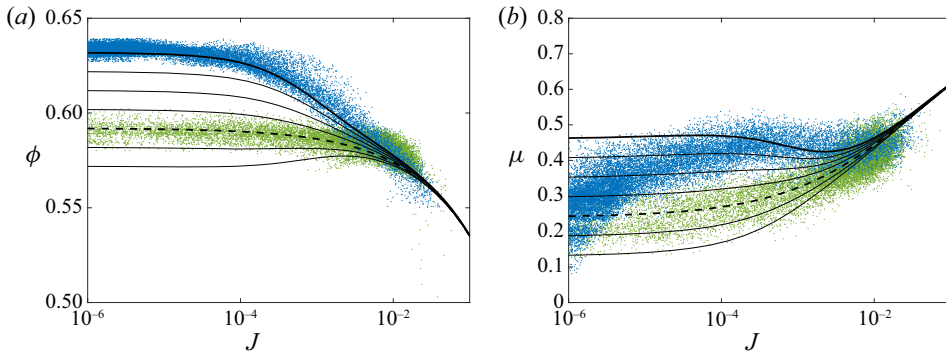


Figure 11. Comparison of the coarse-graining results reported in figure 9 for $\phi_i = 0.63$ (blue dots) and $\phi_i = 0.57$ (green dots) with the model (4.7) (lines): (a) ϕ as a function of J and (b) μ as a function of J . Dashed lines correspond to the equilibrium rheological model, i.e. $\phi_i = \phi_c$, while solid lines show the out-of-equilibrium model for $\phi_i = [0.57 : 0.01 : 0.63]$.

5. Discussion

A simple phenomenological model is proposed in an attempt to provide a link between the rheological models obtained in the previous section and the morphology of the final state of the collapse. If the inertial acceleration of the granular slumping is not a dominant contribution of the collapse, which seems reasonable for immersed configurations and more particularly for small a , the final state is controlled by a balance between the macro pressure gradient, linked to the height gradient, and the friction term close to threshold. In other words, we suppose a quasi-static evolution of the collapse preventing the granular medium spreading further than its state at the threshold of motion. Obviously more complex situations could be imagined, particularly when increasing a , but it is shown here that this assumption is sufficient to explain the influence of (St, ϕ_i) discussed so far. Assuming the final deposit to have a trapezoidal shape, one simply obtains

$$\tan \alpha = \mu \quad \text{and} \quad \frac{L_f - L_i}{L_i} = \frac{a}{2\mu}, \quad (5.1a,b)$$

with μ some effective friction coefficient at the macroscopic scale to be determined. Then the deposit only depends on the model prescribed to μ for a given a . According to the results obtained in the previous section, the friction parameter, even at threshold, can vary for varying St and ϕ_i . This leads to a finite interval of possible deposit slope, even for a quasi-static situation. Based on (4.6) and (4.7), we propose here to write this friction parameter as

$$\mu = \mu_c(St) + b(\phi_i - \phi_c) \frac{\dot{\Gamma}^{-1}}{t_\phi}, \quad (5.2)$$

with t_ϕ a time scale associated with the evolution of ϕ , from ϕ_i to ϕ_c during the initiation stage, and $\dot{\Gamma}^{-1}$ is a macroscopic time scale of deformation of the granular medium.

Defining these two time scales is not straightforward for such a predictive model, as different stages of the collapse have been shown to highlight different behaviours. A key point is thus to anticipate the stage controlling the final deposit. We thus base their definition on the observations extracted from figures 5 and 10. In particular, we have shown that ϕ_i influences the final deposit mostly at small St . Moreover, ϕ_i has been shown to affect the rheological behaviour during the initiation stage. We thus anticipate that the initiation

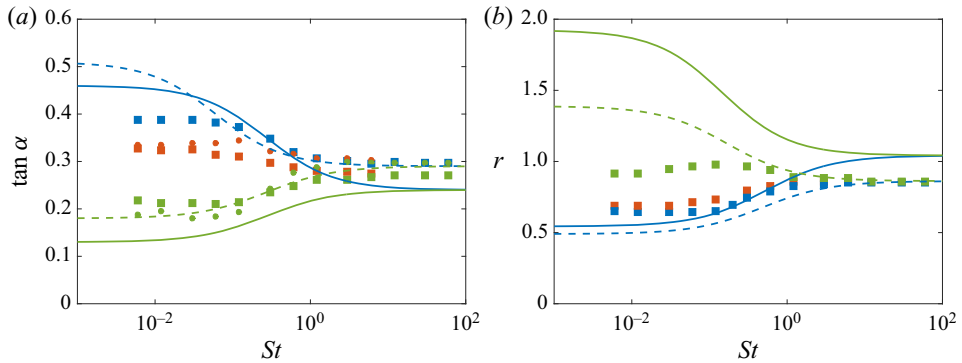


Figure 12. Geometrical characteristics of the final deposit: (a) the deposit angle and (b) the dimensionless spreading length $r = (L_f - L_i)/L_i$ as functions of St and different ϕ_i (green, $\phi_i = 0.57$; red, $\phi_i = 0.59$; and blue, $\phi_i = 0.63$). Symbols correspond to mesoscale VANS/DEM simulations (reported from figure 5a,b; see the corresponding caption for details) and lines are model (5.3) with $\mu_c(St \rightarrow 0) = 0.24$ (solid lines) and $\mu_c(St \gg 1) = 0.29$ (dashed lines).

stage is of main importance at small St while it probably does not affect much the final state at large St . Accordingly, $\dot{\Gamma}^{-1}/t_\phi$ should be order one at small St and decreases with increasing St .

According to the definition of t_ϕ as given in the previous section, i.e. a microscopic time scale of rearrangement, we write $t_\phi = \eta/\Delta\rho gH_i + \beta d\sqrt{\rho_p/\Delta\rho gH_i}$, obtained for a granulostatic pressure over the column height, and accounting for a viscous to free-fall transition. Note that β is used here as in the definition of K for the sake of simplicity, as the transition parameter from the viscous to the free-fall regime. Then t_ϕ accounts for the difference in time scale for rearrangement depending on the state, viscous versus free-fall. According to the previous discussion, this time scale should be compared to a viscous time scale of macroscopic deformation of the granular medium, then $\dot{\Gamma}^{-1}/t_\phi$ would actually be of order one at small St . This therefore implies that the relevant deformation accounting for dilatancy/compaction of the initial granular column is associated with a viscous scale. It is thus written as $\dot{\Gamma}^{-1} = \eta/\Delta\rho gH_i$, imposed by the balance between pressure gradient and viscous shear. This leads to

$$\mu = \mu_c(St) + b(\phi_i - \phi_c) \frac{1}{1 + \beta St\sqrt{H_i/d}}. \tag{5.3}$$

Figure 12 shows a comparison of this model for both the spreading length and final deposit angle with numerical results. Here, each line corresponds to the St dependence of the final deposit through the dilatancy/compaction term in (5.3), μ_c being the value obtained in figure 8(b) either at large St (dashed lines) or at small St (solid lines). Even if the quantitative agreement seems poor, it clearly captures the trend of the evolution of the final state depending on (St, ϕ) . Then the ingredient to understand and predict the final deposit seems to be captured. Certainly, the specific evolution of the collapse and the different stages observed depending on (St, ϕ) have not been explicitly considered here, as, for instance, loose and dense configurations do not have a similar initiation stage and resting stage. A better description and understanding of the physics of immersed granular collapse would thus require an intermediate description between the mesoscale approach and such a simple model. In particular, Euler–Euler simulations would be necessary to

show the relevance of the local rheology obtained in the previous sections in the concept of continuum modelling. A full shallow-layer prediction on the unsteady flow could then be used to confirm the pertinent time scales required for a simple predictive model as discussed here.

6. Conclusion

Numerical simulations of an immersed granular collapse have been reported. The objective of the paper was to provide a characterization of immersed granular collapse with respect to the Stokes number St and the volume fraction of the initial column ϕ_i , which have been reported as the two parameters controlling the dynamics and the final deposit in experimental studies. The relative influences of these two parameters have been studied here using numerical simulations at a scale referred to as the mesoscale according to the scale of the fluid resolution, the granular phase being solved using a Lagrangian DEM approach. This method has been referred to as the VANS/DEM approach.

The influence of the two control parameters (St, ϕ_i) that characterize the immersed granular column in this case can thus be investigated. First, their influences on the dynamics and the final deposit have been considered. In particular, the influence of ϕ_i is quite significant on the dynamics of the flow at small St , i.e. in the viscous regime as reported by Rondon *et al.* (2011), but tends to disappear at large St , probably explaining why its influence has mostly not been reported in dry granular flows. However, when $St \rightarrow 0$, varying ϕ_i can lead to very distinct behaviours, as it can enhance the mobility of the granular material compared to the dry case for small ϕ_i , while the spreading length decreases with decreasing St for large ϕ_i .

These simulations have then been used to provide the proposed viscoplastic rheological models, based on models obtained for steady configurations in the literature. In particular, the well-known $\mu(I)$ rheology has been considered as the rheological base model, but accounting for both an extension to the inertial number K as defined in Trulsson *et al.* (2012) unifying free-fall and viscous granular flows, and a dilatancy ψ model. In particular, the rheology is characterized here by $\phi(K)$ and $\mu(K)$ obtained using a coarse-graining method. The rheological behaviour has been studied by separating two stages of the collapse: an initiation stage dominated by a dilatancy/compaction process and a resting stage assumed as being characterized by an equilibrium rheological law as in the steady configuration. The initiation stage has been shown to be strongly influenced by ϕ_i . Accordingly, an extension of the equilibrium rheological model accounting for the dilatancy/compaction effect has been proposed, referring to out-of-equilibrium rheological states. This has been shown to be pertinent for the configuration studied in this paper. However, it would have to be confirmed in other situations, as the assumptions made here to obtain the model could be relevant only for the considered flow. The resting stage has been shown to slightly depend on St . However, this latter observation remains unclear, as it has no clear physical support. This would deserve specific attention, particularly on the process of compaction during the resting stage, probably influenced by St .

To finish with, a link between this rheology and the shape of the final deposit has been highlighted assuming a quasi-static evolution state towards an equilibrium between the pressure gradient and a friction term at threshold. A comparison with the numerical results shows that the influence of (St, ϕ_i) on the final state can be captured by this simple model. A more refined model would be required to improve the quantitative evolution of the final state in the (St, ϕ_i) parameter space.

Supplementary material. Supplementary material is available at <https://doi.org/10.1017/jfm.2020.1088>.

Acknowledgements. The authors thank A. Pedrono and T. Bonometti for their support in the development of the immersed boundary method/DEM and the VANS/DEM. We acknowledge the anonymous reviewers, whose thorough reviews helped to significantly improve the manuscript. Some of the computational time was provided by the ‘Groupement Scientifique CALMIP’ (project P1027), the contributions of which are greatly appreciated.

Funding. This study has been supported by the ‘Agence Nationale de la Recherche’ in the frame of the project ANR MODSED No. ANR-12-JS09-0012.

Author ORCID.

 Laurent Lacaze <https://orcid.org/0000-0002-4945-7445>.

REFERENCES

- BALMFORTH, N.J. & KERSWELL, R.R. 2005 Granular collapse in two dimensions. *J. Fluid Mech.* **538**, 399–428.
- BARAN, O., ERTAŞ, D., HALSEY, T.C., GREST, G.S. & LECHMAN, J.B. 2006 Velocity correlations in dense gravity-driven granular chute flow. *Phys. Rev. E* **74** (5), 051302.
- BARKER, T. & GRAY, J.M.N.T. 2017 Partial regularisation of the incompressible $\mu(I)$ -rheology for granular flow. *J. Fluid Mech.* **828**, 5–32.
- BAUMGARTEN, A.S. & KAMRIN, K. 2019 A general fluid–sediment mixture model and constitutive theory validated in many flow regimes. *J. Fluid Mech.* **861**, 721–764.
- BOUGOUIN, A. & LACAZE, L. 2018 Granular collapse in a fluid: different flow regimes for an initially dense-packing. *Phys. Rev. Fluids* **3** (6), 064305.
- CABRERA, M. & ESTRADA, N. 2019 Granular column collapse: analysis of grain-size effects. *Phys. Rev. E* **99** (1), 012905.
- CASSAR, C., NICOLAS, M. & POULIQUEN, O. 2005 Submarine granular flows down inclined planes. *Phys. Fluids* **17** (10), 103301.
- CHARRU, F., BOUTELOUP, J., BONOMETTI, T. & LACAZE, L. 2016 Sediment transport and bedforms: a numerical study of two-phase viscous shear flow. *Meccanica* **51** (12), 3055–3065.
- COURRECH DU PONT, S., GONDRET, P., PERRIN, B. & RABAUD, M. 2003 Granular avalanches in fluids. *Phys. Rev. Lett.* **90** (4), 044301.
- CROSTA, G.B., IMPOSIMATO, S. & RODDEMAN, D. 2009 Numerical modeling of 2-D granular step collapse on erodible and nonerodible surface. *J. Geophys. Res.* **114** (F3).
- DA CRUZ, F., EMAM, S., PROCHNOW, M., ROUX, J.-N. & CHEVOIR, F. 2005 Rheophysics of dense granular materials: discrete simulation of plane shear flows. *Phys. Rev. E* **72** (2), 021309.
- DAERR, A. & DOUADY, S. 1999 Sensitivity of granular surface flows to preparation. *Europhys. Lett.* **47** (3), 324.
- DEGAETANO, M., LACAZE, L. & PHILLIPS, J.C. 2013 The influence of localised size reorganisation on short-duration bidispersed granular flows. *Eur. Phys. J. E* **36** (4), 36.
- GDR MID1 2004 On dense granular flows. *Eur. Phys. J. E* **14** (4), 341–365.
- GIROLAMI, L., HERGAULT, V., VINAY, G. & WACHS, A. 2012 A three-dimensional discrete-grain model for the simulation of dam-break rectangular collapses: comparison between numerical results and experiments. *Granul. Matt.* **14** (3), 381–392.
- GOLDHIRSCH, I. & GOLDENBERG, C. 2002 On the microscopic foundations of elasticity. *Eur. Phys. J. E* **9** (3), 245–251.
- GONDRET, P., LANCE, M. & PETIT, L. 2002 Bouncing motion of spherical particles in fluids. *Phys. Fluids* **14** (2), 643–652.
- GUAZZELLI, E. & POULIQUEN, O. 2018 Rheology of dense granular suspensions. *J. Fluid Mech.* **852**, P1.
- IONESCU, I.R., MANGENEY, A., BOUCHUT, F. & ROCHE, O. 2015 Viscoplastic modeling of granular column collapse with pressure-dependent rheology. *J. Non-Newtonian Fluid Mech.* **219**, 1–18.
- IZARD, E., BONOMETTI, T. & LACAZE, L. 2014 Modelling the dynamics of a sphere approaching and bouncing on a wall in a viscous fluid. *J. Fluid Mech.* **747**, 422–446.
- JACKSON, R. 2000 *The Dynamics of Fluidized Particles*. Cambridge University Press.
- JING, L., YANG, G.C., KWOK, C.Y. & SOBRAL, Y.D. 2018 Dynamics and scaling laws of underwater granular collapse with varying aspect ratios. *Phys. Rev. E* **98** (4), 042901.
- JING, L., YANG, G.C., KWOK, C.Y. & SOBRAL, Y.D. 2019 Flow regimes and dynamic similarity of immersed granular collapse: a CFD-DEM investigation. *Powder Technol.* **345**, 532–543.

- JOP, P., FORTERRE, Y. & POULIQUEN, O. 2006 A constitutive law for dense granular flows. *Nature* **441** (7094), 727–730.
- LACAZE, L. & KERSWELL, R.R. 2009 Axisymmetric granular collapse: a transient 3D flow test of viscoplasticity. *Phys. Rev. Lett.* **102** (10), 108305.
- LACAZE, L., PHILLIPS, J.C. & KERSWELL, R.R. 2008 Planar collapse of a granular column: experiments and discrete element simulations. *Phys. Fluids* **20** (6), 063302.
- LAGRÉE, P.-Y., STARON, L. & POPINET, S. 2011 The granular column collapse as a continuum: validity of a two-dimensional Navier–Stokes model with a μ (i)-rheology. *J. Fluid Mech.* **686**, 378–408.
- LAJEUNESSE, E., MANGENEY-CASTELNAU, A. & VILOTTE, J.-P. 2004 Spreading of a granular mass on a horizontal plane. *Phys. Fluids* **16** (7), 2371–2381.
- LAJEUNESSE, E., MONNIER, J.B. & HOMSY, G.M. 2005 Granular slumping on a horizontal surface. *Phys. Fluids* **17** (10), 103302.
- LUBE, G., HUPPERT, H.E., SPARKS, R.S.J. & FREUNDT, A. 2005 Collapses of two-dimensional granular columns. *Phys. Rev. E* **72** (4), 041301.
- LUBE, G., HUPPERT, H.E., SPARKS, R.S.J. & HALLWORTH, M.A. 2004 Axisymmetric collapses of granular columns. *J. Fluid Mech.* **508**, 175–199.
- MANGENEY, A., ROCHE, O., HUNGR, O., MANGOLD, N., FACCANONI, G. & LUCAS, A. 2010 Erosion and mobility in granular collapse over sloping beds. *J. Geophys. Res.* **115**, F03040.
- MANGENEY-CASTELNAU, A., BOUCHUT, F., VILOTTE, J.-P., LAJEUNESSE, E., AUBERTIN, A. & PIRULLI, M. 2005 On the use of saint venant equations to simulate the spreading of a granular mass. *J. Geophys. Res.* **110**, B09103.
- MAURIN, R., CHAUCHAT, J., CHAREYRE, B. & FREY, P. 2015 A minimal coupled fluid-discrete element model for bedload transport. *Phys. Fluids* **27** (11), 113302.
- PÄHTZ, T. & DURÁN, O. 2018 Universal friction law at granular solid-gas transition explains scaling of sediment transport load with excess fluid shear stress. *Phys. Rev. Fluids* **3** (10), 104302.
- PAILHA, M. & POULIQUEN, O. 2009 A two-phase flow description of the initiation of underwater granular avalanches. *J. Fluid Mech.* **633**, 115–135.
- PHILLIPS, J.C., HOGG, A.J., KERSWELL, R.R. & THOMAS, N.H. 2006 Enhanced mobility of granular mixtures of fine and coarse particles. *Earth Planet. Sci. Lett.* **246** (3–4), 466–480.
- RICHARDSON, J.F. & ZAKI, W.N. 1954 The sedimentation of a suspension of uniform spheres under conditions of viscous flow. *Chem. Engng Sci.* **3** (2), 65–73.
- ROCHE, O., ATTALI, M., MANGENEY, A. & LUCAS, A. 2011 On the run-out distance of geophysical gravitational flows: insight from fluidized granular collapse experiments. *Earth Planet. Sci. Lett.* **311** (3–4), 375–385.
- RONDON, L., POULIQUEN, O. & AUSSILLOUS, P. 2011 Granular collapse in a fluid: role of the initial volume fraction. *Phys. Fluids* **23** (7), 073301.
- ROUX, S. & RADJAI, F. 1998 Texture-dependent rigid-plastic behavior. In *Physics of Dry Granular Media* (ed. H.J. Herrmann, J.-P. Hovi & S. Luding), pp. 229–236. Springer.
- STARON, L. & HINCH, E.J. 2005 Study of the collapse of granular columns using two-dimensional discrete-grain simulation. *J. Fluid Mech.* **545**, 1–27.
- STARON, L. & HINCH, E.J. 2007 The spreading of a granular mass: role of grain properties and initial conditions. *Granul. Matt.* **9** (3–4), 205–217.
- TOPIN, V., MONERIE, Y., PERALES, F. & RADJAI, F. 2012 Collapse dynamics and runout of dense granular materials in a fluid. *Phys. Rev. Lett.* **109** (18), 188001.
- TRULSSON, M., ANDREOTTI, B. & CLAUDIN, P. 2012 Transition from the viscous to inertial regime in dense suspensions. *Phys. Rev. Lett.* **109** (11), 118305.
- WEINHART, T., THORNTON, A.R., LUDING, S. & BOKHOVE, O. 2012 Closure relations for shallow granular flows from particle simulations. *Granul. Matt.* **14** (4), 531–552.
- ZENIT, R. 2005 Computer simulations of the collapse of a granular column. *Phys. Fluids* **17** (3), 031703.
- ZHANG, D.Z. & PROSPERETTI, A. 1997 Momentum and energy equations for disperse two-phase flows and their closure for dilute suspensions. *Intl J. Multiphase Flow* **23** (3), 425–453.